



Surface, textural and catalytic properties of pyridinium hydrogen sulfate ionic liquid heterogenized on activated carbon carrier



Ivaylo Tankov^{a,*}, Hristo Kolev^b, Georgi Avdeev^c

^a University "Prof. Dr. Assen Zlatarov" Burgas, 8010, Bulgaria

^b Institute of Catalysis, Bulgarian Academy of Sciences, Bulgaria

^c Institute of Physical Chemistry, Bulgarian Academy of Sciences, Bulgaria

ARTICLE INFO

Article history:

Received 13 April 2021

Revised 14 July 2021

Accepted 4 August 2021

Available online 9 August 2021

Keywords:

Heterogenized pyridinium ionic liquids

Activated carbon

Surface characterization

Textural properties

Catalytic performance

ABSTRACT

Pyridinium hydrogen sulfate ionic liquid (PHS) heterogenized on activated carbon (AC) is investigated for the first time in the current paper. For that purpose, the *x*PHS/AC (*x* = 8, 17, 33 and 66 wt%) samples are analyzed by a number of physicochemical methods such as N₂ adsorption–desorption measurements, X-ray diffraction, X-ray photoelectron spectroscopy and Fourier transform infrared spectroscopy. Catalytic activity and reusability of *x*PHS/AC are evaluated in the reaction of butyl acetate synthesis. Effect of the reaction temperature and catalyst loading on the butyl acetate yield are examined in this work as well. Important thermodynamic parameters such as equilibrium constant, activation energy, Gibbs free energy and activation energy barrier for the reaction of butyl acetate synthesis in the presence of *x*PHS/AC are determined.

Textural characterization revealed that *x*PHS/AC are mixed micro-mesoporous materials. The PHS heterogenization on AC affects both ionic liquid and support phases due to a surface PHS–AC interaction. FT-IR and XPS showed that this interaction is: (i) mainly expressed as a close contact between the pyridinium cation and the functional groups on the AC surface and (ii) electrostatic in nature. The existence of a PHS–AC interaction is found to be responsible for the formation of surface PHS particles of various size. However, the catalytic activity of *x*PHS/AC is established to be affected by the surface active phase amount, but not the PHS particle size.

© 2021 Elsevier B.V. All rights reserved.

1. Introduction

Ionic liquids (ILs) are compounds of considerable interest due to their unique properties such as a wide electrochemically stable window [1], good electric conductivity [2], high ionic mobility [3], a broad range of room temperature liquid compositions [4], negligible vapor pressure [5], moderated chemical and thermal stability [6,7]. Hence, many of these materials have been applied in different fields ranging from electrochemistry [8] and organic synthesis [9] to separation approaches [10] and production of nanostructured materials [11].

Although the pyridinium hydrogen sulfate (PHS) and its derivatives are one of the simplest, low cost and easily-producible Brønsted acidic ionic liquids, their catalytic activity is mainly investigated as homogeneous catalytic systems in different types of acid-catalyzed organic reactions [12–14]. For example, the ion pair [PyrSO₃H]⁺[HSO₄]⁻ is successfully applied as a recyclable homogeneous catalyst for one-pot synthesis of functionalized

tetrahydropyridines [12]. To study the catalytic behavior of PHS, acetic acid esterification with butanol is carried out by Lunagariya et al. [13] and Tao and co-workers [14]. As a result, values of 55 and 71%, respectively are noted as a butyl acetate yield. However, some disadvantages are reported when ionic liquids are used as homogeneous catalysts: (i) large amounts of ILs are required for high reactants conversion, (ii) high ILs viscosity hinders the mass transfer, (iii) IL catalyst separation from the reaction products is a difficult task [6]. To overcome these drawbacks, ILs immobilization on solid supports is extensively studied [7]. While various solids such as aluminosilicates [15,16], metal oxides (Fe₂O₃, SiO₂, Al₂O₃) [17–19], rice husk ash [20], chloromethylated polystyrene [21] are reported as effective carriers for ionic liquids in different fields, a number of works are focused on the activated carbon as an ILs support due to its high abundance, large specific surface area and highly developed porosity structure [22–26].

The supported ionic liquid (SILs) catalysts combine the advantages of the ILs and those of the solid support. Compared with pure ILs, SILs offer further benefits such as easy separation, reusability and application in fixed or fluidized bed reactors. It should be

* Corresponding author.

further emphasized that even a very low solubility of the catalyst in the flowing liquid media will make long term stability of the SILs catalyst system impossible due to slow but steady leaching. Moreover, almost identical catalytic activity between the SILs and their homogenous counterparts is shown as well [18]. Different approaches such as solid supports impregnation with IL, formation of interface covalent interactions between IL and carrier, IL confinement in the support material and copolymerisation of IL with a suitable monomer are offered for SILs. Surface covalent bonds between the IL and the support may be formed even when the SILP is obtained by impregnation [27]. Non-covalent interactions of functional groups with solid surfaces are also detected by IR measurements [28].

It is generally accepted that the catalytic properties of a heterogeneous catalyst are notably affected by the carrier nature due to a surface active phase-support interaction [29]. Therefore, to predict the properties of SILs catalysts and choose one for a specific application, a detailed analysis on the IL-support interaction needs to be carried out. The ILs immobilization degree on a solid support surface as well as the ILs-support interaction is successfully investigated by different analytical techniques, namely N₂ adsorption-desorption measurement (S_{BET}), X-ray diffraction (XRD), X-ray photoelectron spectroscopy (XPS), spectroscopy in the ultraviolet and visible regions (UV-vis), Fourier transform infrared spectroscopy (FT-IR) and thermogravimetric analysis (TGA).

The current work is a first attempt for investigation the surface, textural and catalytic properties pyridinium hydrogen sulfate ionic liquid heterogenized on activated carbon (xPHS/AC). For physicochemical characterization of the xPHS/AC systems, a combination of analytical methods (XRD, S_{BET}, XPS and FT-IR) is applied. The catalytic activity of xPHS/AC is compared using the reaction of butyl acetate synthesis. The results obtained are expected to be useful for future experimental studies on the structure-activity relationship in different types of heterogenized ionic liquids.

2. Experimental section

2.1. Synthesis of PHS

Pyridine (2.13 g, 0.0269 mol) and ultra clean water (1.45 g, 0.0807 mol) are loaded into a 0.020 l three-necked flat bottom reactor, equipped with a magnetic stirring, a reflux condenser and a thermometer. The aqueous solution of pyridine is stirred at room temperature for 0.5 h, where after the temperature is reduced to 5 °C. Then, H₂SO₄ (2.64 g, 0.0269 mol) is added dropwise over a period of 1.5 h under vigorous stirring. The reaction mixture is stirred at reflux for a period of 5 h at 80 °C. For solvent removing, the aqueous solution of pyridinium hydrogen sulfate is distilled at 70 °C under reduced pressure (0.050 MPa) and the product is dried at the same conditions for 8 h until the residue mass remained constant. After cooling, the colorless solid is washed three times with diethyl ether (0.100 l) and dried under vacuum (0.050 MPa) at 80 °C for 12 h.

2.2. Heterogenization of PHS

The xPHS/AC samples are obtained by wetness impregnation of activated carbon (3 g, Merck) with an aqueous solution of PHS. The activated carbon is added to a solution of a known PHS amount (8, 17, 33 and 66 wt% with respect to the mass of support) and the mixture is intensively stirred (1000 rpm) at ambient temperature for 30 h. The water is slowly removed in a rotary evaporator at 70 °C and reduced pressure (0.010 MPa). The solids (xPHS/AC, where x = 8, 17, 33 and 66 wt%) are dried at 110 °C and 0.1 MPa for 12 h.

2.3. Physicochemical characterization of xPHS/AC

XRD analysis is performed by a computerized Seifert 3000XRD diffractometer using Cu K α ($\lambda = 0.15406$ nm) radiation and a PW 2200 Bragg-Brentano $\theta/2\theta$ goniometer equipped with a bent-graphite monochromator and an automatic slit. Diffraction peaks are recorded in a 2θ range of 10–90° with step size of 0.033 and step scan of 10.0 s. Phase identification is carried out by comparison with database cards. The crystallite size of PHS nanoparticles is calculated from the full width at half maximum (FWHM) of the diffraction peaks using Debye-Scherrer's equation:

$$D = \frac{k\lambda}{\beta \cos\theta} \quad (1)$$

where, "D" is the average crystalline dimension perpendicular to the surface of the specimen, " λ " is the wavelength of used X-ray, "k" is Scherrer's constant (0.9), " β " is the FWHM intensity of a Bragg reflection excluding instrumental broadening and " θ " is the Bragg diffraction angle. The values of the β and θ parameters from the XRD peak are estimated by Gaussian fitting.

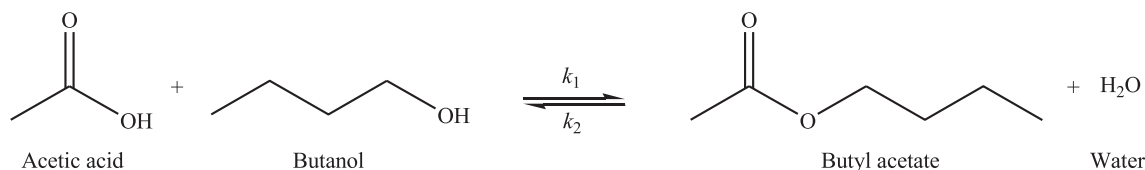
Textural characterization is evaluated from the N₂ adsorption-desorption isotherms, determined at –196 °C on an automatic apparatus Surfer sorption analyzer (Thermo Scientific). The surface area of the samples is determined by the BET method using data from the adsorption isotherms in the range of relative pressures (P/P₀) from 0.05 to 0.28 (for isotherms type IV). The total pore volume, known as volume of Gurvich, is determined based on the volume of adsorbate V_{0.98}, recorded on the desorption branch of the adsorption isotherm at P_i/P₀ of 0.98. The micropore volume is calculated by the Dubinin-Radushkevich equation up to P/P₀ ≤ 0.15. The pore diameters are obtained by applying the Nonlocal density functional theory (NLDFT) on N₂ adsorption data.

Vibrational (FT-IR) frequencies are recorded in the middle infrared region (4000–400 cm⁻¹) by means of a Nicolet iS 50 Thermo Scientific FT-IR spectrophotometer equipped with DTGS KBr detector (4 cm⁻¹) at scan's number of 32.

XPS analysis is carried out using ESCALAB MkII (VG Scientific) electron spectrometer at a base pressure in the analysis chamber of 5 × 10⁻¹⁰ mbar (during the measurement 10⁻⁸ mbar), using AlK α X-ray source (excitation energy 1486.6 eV). The pass energy of the hemispherical analyzer is 20 eV, 6 mm slit widths (entrance/exit). The instrumental resolution measured as the full width at a half maximum (FWHM) of the Ag 3d_{5/2}, photoelectron peak is 1 eV. The energy scale is corrected to the C 1s – peak maximum at 285.0 eV for electrostatic charging. The processing of the measured spectra includes a subtraction of X-ray satellites and Shirley-type background [30]. The peak positions and areas are evaluated by a symmetrical Gaussian-Lorentzian curve fitting. The accuracy of the BE values is ± 0.2 eV. The relative concentrations of the different chemical species are determined based on normalization of the peak areas to their photoionization cross-sections, calculated by Scofield [31].

2.4. Batch experiment

For butyl acetate synthesis (Scheme 1), acetic acid (8.34 g, 0.1388 mol) and a catalyst (10 wt%, with respect to the mass of substrate) are placed in a three-necked round bottom flask of 0.100 l capacity. The latter is equipped with a condenser, a port for sample withdrawal and a thermometer. Mixing of the reaction fluids is performed by a magnetic stirrer. Once the desired reaction temperature (80 °C) is reached, an equimolar amount (10.29 g, 0.1388 mol) of 1-butanol, separately heated to the set reaction temperature (80 °C) is added into the reactor. This time is considered as zero reaction time (t = 0). The reaction progress is



Scheme 1. Butyl acetate synthesis in the presence of xPHS/AC catalysts.

monitored by a GC analysis. At regular intervals of time (10 min), a sample (1 ml) is withdrawn and cooled in an ice bath. The reaction mixture is analyzed by GC 7890A (Agilent Technologies) equipped with a flame ionization detector and a capillary column HP-INNOWAX, 30 m × 0.32 mm × 0.25 μm. High purity helium at a flow rate of 0.0015 l/min is used as a carrier gas. The oven temperature is programmed at 70 °C for 2 min and then it is raised from an initial value of 70 to 190 °C at a ramp rate of 5 °C/min. The injector and detector temperature are maintained at 250 and 300 °C, respectively. The analytical uncertainty of GC is less than 4%, which is in accordance with the acceptable limits. The acetic acid conversion is calculated according to Eq. (2). It should be noted that side reactions such as alcohol dehydration are not detected.

$$X_A = \frac{C_A - C_{A_0}}{C_{A_0}} \quad (2)$$

where, X_A is the acetic acid conversion, C_{A_0} denotes the initial concentration (mol/l) of acetic acid and C_A corresponds to the acetic acid concentration (mol/l) at a given reaction time (t , min).

3. Results and discussion

3.1. Phase identification and textural properties

For identification of the phases present in activated carbon and heterogenized pyridinium hydrogen sulfate ionic liquid, a XRD analysis is applied. The XRD patterns of AC and xPHS/AC systems

are shown in Fig. 1A. For comparison, the X-ray diffractogram for the non-heterogenized (bulk) ionic liquid (PHS) is added as well.

The X-ray diffractogram of AC sample showed two broad diffraction peaks with 2θ maxima at 23.5° and 43.4° and a sharp one $2\theta = 26.5^\circ$ due to graphitic carbon (JCPDS, 75–1621). In details, the XRD patterns at $2\theta = 23.5^\circ$ and 26.5° correspond to the reflection of (002), while the peak at a higher diffraction angle expresses the (100) lattice plane [32,33]. The broad shape of the XRD patterns at $2\theta = 23.5^\circ$ and 43.4° indicates that the activated carbon structure is notably amorphous in nature. However, the well-defined diffraction peak at $2\theta = 26.5^\circ$ implies the presence of a crystal phase of graphite. Using Eq. (1), a value of 44.7 nm is calculated as an average size (D_{002}) of the graphite particles (Table 1). It should be noted that the findings in this work are in a good agreement with the data reported in the literature [34–36]. For example, the preparation of synthetic graphite materials with hierarchical pores from lignite by one-step impregnation and their characterization as dye absorbents is reported in a paper of Qiu et al. [35]. The description of phase composition via XRD revealed a sharp diffraction peak at $2\theta = 26.5^\circ$ referred as a crystal phase of graphite. In another work, the X-ray diffraction analysis on activated carbons obtained from waste materials impregnated with H_3PO_4 established a broad fuzzy peak at 2θ within 15°–30° related to the (002) lattice plane. Based on it, an amorphous carbon structure is mainly denoted [36]. The XRD results for AC carrier in this paper are found to be practically identical to those presented by Sibirian et al. [37], where a new route for synthesis of graphene nano sheets is offered. The authors detected a sharp and tight peak ($2\theta = 26.5^\circ$ and 23.8°) in the graphite diffractogram which corresponds to the

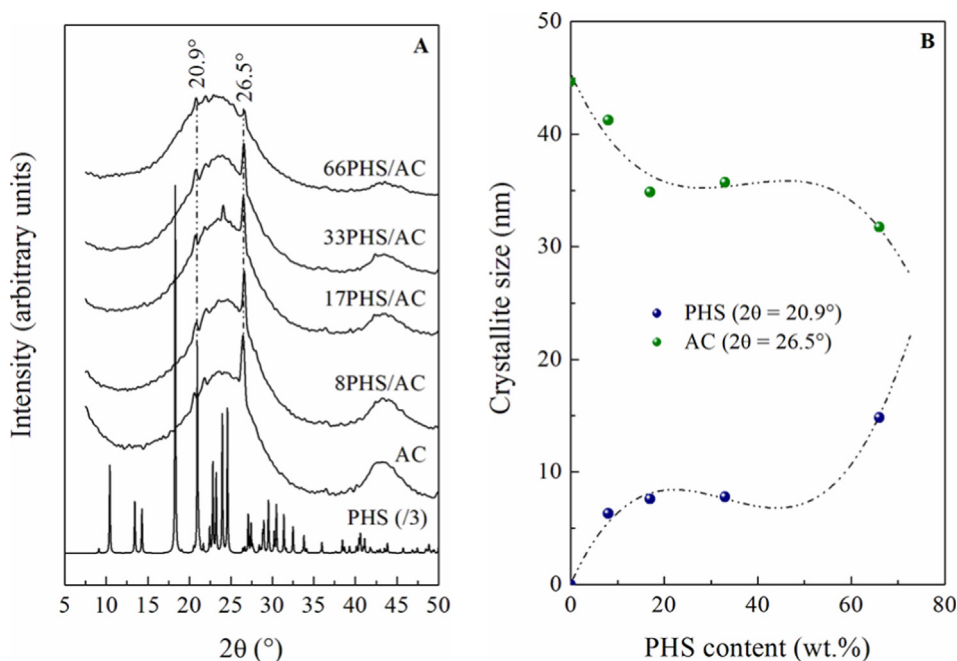


Fig. 1. X-ray diffractograms of PHS, AC and xPHS/AC (A) and a size of crystallites in xPHS/AC as a function of the ionic liquid content (B).

Table 1
Textural properties of AC and xPHS/AC samples.

Parameter	Sample				
	AC	8PHS/AC	17PHS/AC	33PHS/AC	66PHS/AC
S_{BET} (m ² /g)	864	473	175	113	10
V_{total} (cm ³ /g)	0.6400	0.4701	0.2722	0.2364	0.0611
V_{meso} (cm ³ /g)	0.3091	0.2846	0.2084	0.1957	0.0566
V_{micro} (cm ³ /g)	0.3309	0.1855	0.0638	0.0407	0.0045
D_{020} (nm)	–	6.3	7.6	7.8	14.8
D_{002} (nm)	44.7	41.3	34.9	35.7	31.8

diffraction line (002). Islam et al. investigated activated carbon synthesized from coconut shell and established that the AC obtained is characterized with an average crystallite size of 42.5 nm [38].

The X-ray diffraction analysis of the non-heterogenized PHS exposed strong peaks appeared at $2\theta = 10.4^\circ, 13.5^\circ, 14.3^\circ, 18.3^\circ, 20.9^\circ, 22.8^\circ, 23.2^\circ, 23.9^\circ$ and 24.6° , which are assigned to the (010), (01 $\bar{1}$), (011), (002), (020), ($\bar{1}\bar{1}\bar{1}$), (1) $\bar{1}\bar{1}$, (11 $\bar{1}$) and (111) lattice planes, respectively (Fig. 1A). The registered XRD positions for the PHS sample in this paper do not differ from these reported in a work of Rogers and Bauer [39], where the crystal structure of the ion pair PHS is firstly reported. For the lattice planes noted above, XRD patterns at 2θ values of $10.4^\circ, 13.4^\circ, 14.2^\circ, 18.3^\circ, 20.7^\circ, 22.8^\circ, 23.1^\circ, 23.9^\circ$ and 24.5° are recorded indeed. According to Eq. (1), an average crystallite size (D_{020}) of 141.5 nm is calculated for the bulk ionic liquid.

It is found that the AC impregnation with an aqueous solution of pyridinium hydrogen sulfate changes the XRD profile of the support (Fig. 1A), namely the reflection at 2θ of 26.5° (crystalline graphite) gradually decreases with rising the PHS amount. In addition, PHS crystallites are identified on the AC surface via appearance of XRD pattern at $2\theta = 20.9^\circ$ in the XRD profiles of xPHS/AC. To explain the decreased XRD peak at 26.5° , different reasons such as support amorphization and/or reducing the size of carbon crystallites are introduced. It is well known that the number of parallel layers in a crystalline material decreases during amorphization, i.e. a bigger interlayer spacing (d -spacing) characterizes a low-crystallinity material [40]. Speaking for d -spacing, the diffraction peaks shift to lower angles when it increases. XRD analysis clearly shows that the peak position at $2\theta = 26.5^\circ$ in the X-ray diffractogram of AC remains unchanged after the PHS immobilization. On the other hand, calculations revealed that the AC particles size decreases from 44.7 to 41.3 nm when 8 wt% PHS are heterogenized on the support surface (Fig. 1B, Table 1). Further increasing of the PHS content leads to D_{002} values of 34.9 nm (17PHS/AC), 35.7 nm (33PHS/AC) and 31.8 nm (66PHS/AC). Consequently, the decreased XRD peak intensity at 26.5° is related to a reduced carbon crystallites size, rather than a support amorphization.

Considering the surface interaction as the most important motive for reducing the size of a crystalline particle [20,41,42], it is reasonable to propose that the D_{002} decreasing after PHS heterogenization is due to a surface PHS–AC interaction. However, the D_{002} reducing (from 44.7 to 31.8 nm) is not noticeable, suggesting that the PHS–AC interactions in the xPHS/AC samples are very similar in nature. This is being observed in a greater extent for 17PHS/AC and 33PHS/AC systems. On the other hand, values of 6.3, 7.6, 7.8 and 14.8 nm are found as a PHS particles size for 8PHS/AC, 17PHS/AC, 33PHS/AC and 66PHS/AC samples, respectively (Table 1). Excluding the 17PHS/AC and 33PHS/AC samples (possess practically identical D_{020} values), the PHS particles on the AC support surface become larger with rising the PHS content. It can be explained as follows. When a carrier (AC in this work) is impregnated with moderated amounts of an applied material (PHS in this work), presence of a great number of particles of this material on the carrier surface is expected. These species can migrate on the

support surface forming agglomerates. In other words, the D_{020} values raised with PHS content can be ascribed to the improved ionic liquid amounts used for the xPHS/AC samples synthesis.

To describe the textural properties of AC and xPHS/AC, a N_2 adsorption–desorption study is carried out (Fig. 2). According to the IUPAC classification [43,44], type IV–A isotherms characterize the samples investigated in this work. All the adsorption isotherms show a sharp increase in volume at low pressures. This increase in volume is related to the presence of micropores and is followed by slight increase at the middle ($P/P_0 = 0.42$) of the curve. A H–4 hysteresis loop results at the end of the curve, which is associated with capillary condensation. This is characteristic of materials of microporous nature due to a strong interaction potential between the carbon surface and N_2 . The H–4 hysteresis observed above $P/P_0 = 0.4$ may be due to narrow slit-like pores [45].

Analyzing the textural properties of the non-immobilized AC sample, values of 864 m²/g and 0.6400 cm³/g are detected as a specific surface area (S_{BET}) and a total pore volume (V_{total}), respectively (Table 1). The latter is found to consist of equivalent volumes of mesopores ($V_{\text{meso}} = 0.3091$ cm³/g, 48.3%) and micropores ($V_{\text{micro}} = 0.3309$ cm³/g, 51.7%). However, the impregnation of AC with small amounts (8 wt%) of PHS ionic liquid causes the S_{BET} and V_{total} to decrease by 45.3% and 26.5%, respectively. These effects are related to a process of AC pores filling with PHS during the ionic liquid heterogenization. It should be pointed out that the V_{total} decreasing is mainly due to filling of the AC micropores. For instance, V_{micro} and V_{meso} are reduced by 43.9% (0.1855 cm³/g) and 7.9% (0.2846 cm³/g), respectively. The same tendency is noticed when the 17PHS/AC, 33PHS/AC and 66PHS/AC samples are investigated. Hence, values of 175 m²/g (0.2722 cm³/g), 113 m²/g (0.2364 cm³/g) and 10 m²/g (0.0611 cm³/g) are determined as S_{BET} (V_{total}). It is worth noted when the 66PHS/AC sample is synthesized, the carrier's pores are almost completely filled (V_{total} diminishes by more than 90%) by ionic liquid particles. Thus, a greater PHS amount is expected to present on the AC surface in comparison with the PHS content in the case of 8PHS/AC, 17PHS/AC and 33PHS/AC. This is in accordance with the XRD analysis, where larger in size PHS species are registered on the 66PHS/AC sample surface.

3.2. Surface effects

It was noted above that PHS particles of different size (6.3, 7.6, 7.8 and 14.8 nm) exist on the xPHS/AC surface, attributed to the various ability of the particles to migrate on the support surface. To clarify this, the surface effects in the xPHS/AC samples are investigated by means of FT-IR and XPS methods.

3.2.1. Vibrational analysis

Vibrational spectra of AC, PHS and xPHS/AC samples in the frequency region 500–4000 cm^{−1} are illustrated in Fig. 3. To describe the surface effects in xPHS/AC systems accurately, FT-IR spectra of AC and bulk PHS are firstly investigated. Thus, the infrared profile of AC revealed a broad peak of very low intensity between 550 and 650 cm^{−1} and peaks at 1037, 1113, 1239, 1574, 1722, 3359, 3445,

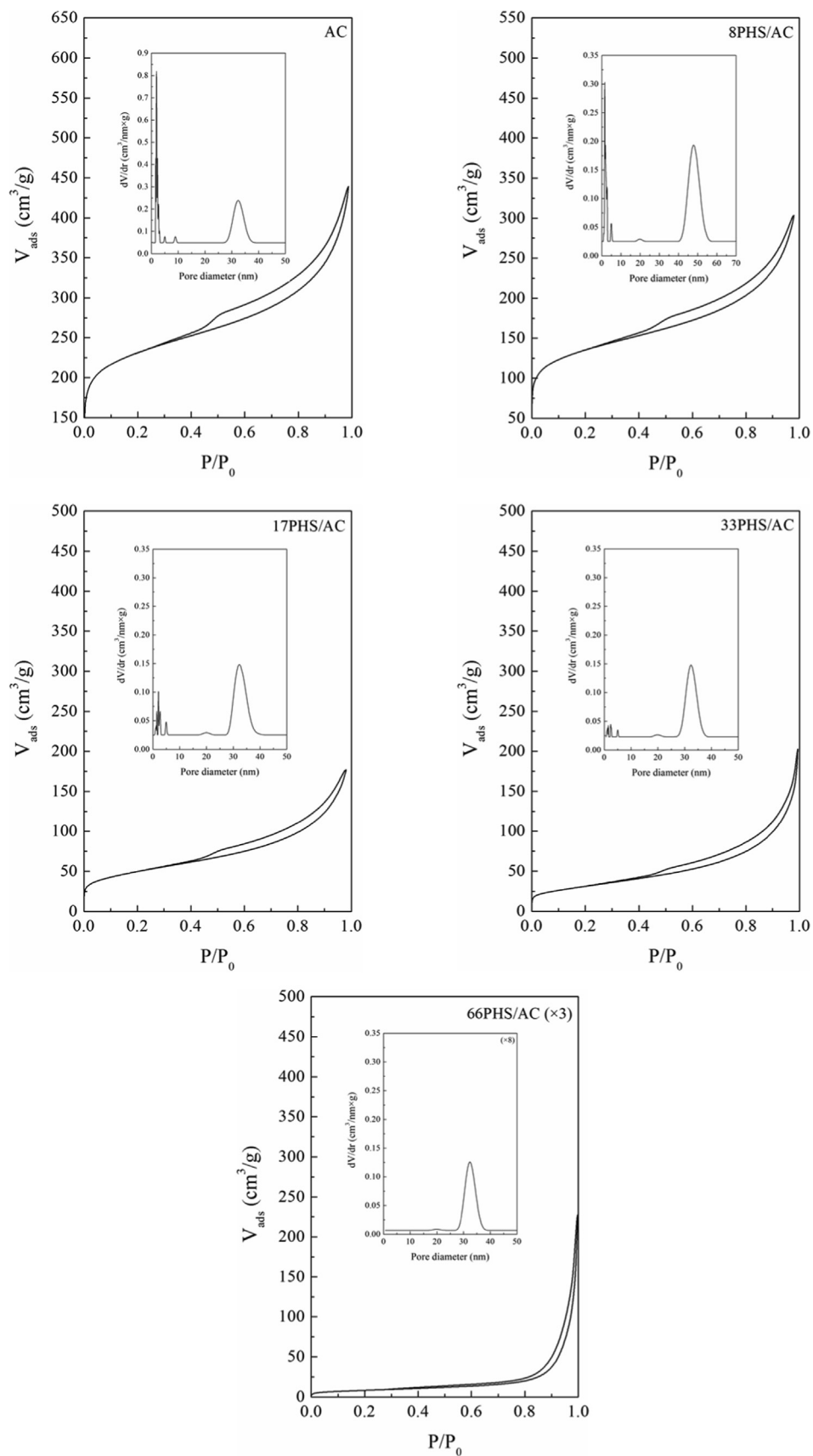


Fig. 2. Adsorption-desorption isotherms and pore size distribution for AC and xPHS/AC samples.

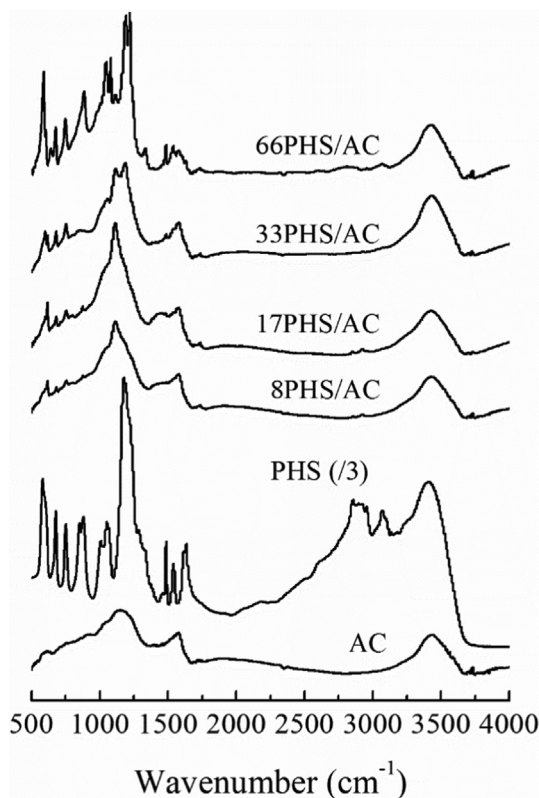


Fig. 3. FT-IR spectra of AC, PHS and xPHS/AC samples in the frequency region 500–4000 cm^{-1} .

3576 and 3729 cm^{-1} , indicating that different types of oxygen-containing functional groups are available on the support surface. The absorbance within 550–650 cm^{-1} is mainly related to vibrations in physisorbed carbon dioxide [46]. This is in accordance with the data presented in a work of Bonelli et al. [47], where a vibrational study of CO_2 adsorption on zeolite Na-ZSM-5 at ambient temperature is conducted. As a result, an infrared band at a wavenumber value of 615 cm^{-1} due to bending vibration in carbon dioxide is registered. In another paper, FT-IR study of CO_2 adsorption in a dynamic copper(ii) benzoate-pyrazine showed an infrared peak at 642 cm^{-1} , assigned to a CO_2 bending mode [48]. However, C–H out-of-plane bending vibrations at wavenumber values between 550 and 650 cm^{-1} are reported for various activated carbons as well [38,49].

While the infrared peaks at 1037 and 1113 cm^{-1} appeared in the FT-IR spectrum of the AC sample are denoted as stretching vibrations in C–O groups [50,51], the band detected at 1239 cm^{-1} is attributed to C–O–C stretching vibration [52]. It should be pointed out that stretching modes due to C–OH [53] and CO_3^{2-} [54] groups on AC surface are described within 1000–1120 cm^{-1} as well. The presence of infrared bands at wavenumber values of 1574 and 1722 cm^{-1} showed stretching vibrations from C = O species [55–57]. It is worth noted that the infrared band at 1574 cm^{-1} is notably broaden on the high-frequency side, probably due to presence of O–H component. It agrees well with the literature data, where appearance bending O–H modes at around 1600 cm^{-1} is widely reported [58]. The broad vibrational band in the region from 3350 to 3730 cm^{-1} represents O–H stretching vibration of hydroxyl functional groups [52]. The low-frequency side of this band (<3400 cm^{-1}) mainly originates from the delocalized O–H stretch modes that are linear combinations of symmetric basis modes of participating water molecules with comparatively large number of hydrogen bonds. The IR intensity in the range

within 3400–3600 cm^{-1} denotes the vibrational transitions of delocalized modes that are linear combinations of either symmetric stretch basis modes or those localized asymmetric stretch basis modes. In light of this, the high frequency shoulder band (>3600 cm^{-1}) is produced by the localized asymmetric O–H stretch modes [59].

FT-IR spectrum of the non-heterogenized PHS ionic liquid showed well-defined peaks at 582, 671, 746, 843, 884, 998, 1056, 1170, 1331, 1482, 1536, 1625, 2870, 3067, 3236 and 3408 cm^{-1} . Among these, the bands located at wavenumber values of 582 and 1331 cm^{-1} are assigned as bending and stretching N–C vibrations, respectively, while those appeared at 998, 1056 cm^{-1} are due to torsion N–C vibrations [60]. In light of this, torsion, symmetric stretching and asymmetric stretching C–C modes are detected at 671, 843 and 884 cm^{-1} , respectively. It should be noted that stretching vibration of the S–OH in the anionic moiety appears at 843 cm^{-1} as well [29]. In this regard, the bands detected at 746 and 1170 cm^{-1} express bending and stretching S–O vibrations in $[\text{HSO}_4]^-$ [61]. Presence of C–H vibrations in the PHS structure are observed at 1482 (symmetric bending), 1536 (asymmetric bending), 3067 (symmetric stretching) and 3236 (asymmetric stretching) cm^{-1} [62]. The infrared bands at 1625 and 2870 cm^{-1} denote protonated pyridine via formation of N–H bond between aromatic ring and hydrogen sulfate fragments [29,63]. Similar to the FT-IR spectrum of AC, the absorption above 3400 cm^{-1} characterizes O–H stretching modes [52,58].

The infrared profiles of xPHS/AC samples in the region from 500 to 1400 cm^{-1} revealed that the infrared bands related to PHS continuously increase with rising of the PHS loading (Fig. 3). This agrees well with the XRD analysis, where the highest PHS content on the AC surface is found in the case of 66PHS/AC sample. Results showed that: (i) the band at 582 cm^{-1} (N–C vibration) in xPHS/AC is considerably more intensive than these at 671, 843 and 884 cm^{-1} (C–C modes), (ii) the ratio between the peaks within 990–1060 cm^{-1} (N–C vibration) and that at 1170 cm^{-1} (S–O vibration) in the FT-IT spectra of xPHS/AC is more noticeable in comparison with the ratio between the same bands in the infrared spectrum of bulk PHS and (iii) the shoulder at 1331 cm^{-1} (N–C vibration) in the FT-IT spectrum of PHS becomes a well-defined peak (being observed in a greater extent for 66PHS/AC) when the xPHS/AC samples are obtained. In other words, it seems that a greater number of N–C interactions, probably in the form of (C–N)_{PHS}⋯(C–C)_{AC} bonds, characterizes the xPHS/AC samples in comparison with the number of N–C interactions in non-heterogenized PHS. In the aforementioned interactions, the (C–N)_{PHS} component denotes C–N bonds in the protonated pyridine ([H–Pyr]⁺ cation) and the (C–C)_{AC} expresses the activated carbon surface. Another indication for an increased number of surface (C–N)_{PHS}⋯(C–C)_{AC} interactions in xPHS/AC samples is obtained analyzing the infrared bands at 1625 and 2870 cm^{-1} (previously denote as N–H vibrations in pure PHS). These are found to be significantly suppressed (decreased in intensity) when the xPHS/AC samples are obtained.

FT-IR analysis showed that the infrared band at 1113 (C–O groups) cm^{-1} in the infrared profiles of 8PHS/AC, 17PHS/AC and 33PHS/AC samples is notably more pronounced in comparison with that of the same band in the infrared spectrum of non-immobilized AC. Superior intensity of this band can be related to the formation of additional C–O groups on the AC surface after PHS heterogenization, most probably a consequence of a cleavage of the hydrogen bond S–O⋯H–N in the PHS structure and formation of surface (S–O)_{PHS}⋯(C–C)_{AC} and (S–O)_{PHS}⋯(C = O)_{AC} interactions. The (S–O)_{PHS} component denotes the S–O fragments in the hydrogen sulfate anion, while the (C–C)_{AC} and (C = O)_{AC} express the AC surface. At first sight, the presence of (S–O)_{PHS}⋯(C–C)_{AC} and (S–O)_{PHS}⋯(C = O)_{AC} interactions suggests that the S–O bond

vibrations in the pure ionic liquid should be hindered in some extent after PHS immobilization AC. In other words, lower S–O bond strength is expected in xPHS/AC samples in comparison with the S–O bond strength in bulk PHS. However, the small difference in the electronegativity of hydrogen and carbon proposes that the S–O bond in PHS and xPHS/AC possesses similar strength. Indeed, the FT-IR spectrum of PHS clearly exposed that the bands related to S–O bond vibrations do not change their position when the xPHS/AC are obtained.

Except more intensive, the infrared band at 1113 cm^{-1} in the FT-IR spectra of 8PHS/AC, 17PHS/AC and 33PHS/AC is found to be considerably broaden (ranges from 950 to 1350 cm^{-1}) with respect to that in the vibrational spectrum of AC. It implies that a surface PHS–AC interaction via formation of $(\text{H}-\text{C})_{\text{PHS}}\cdots(\text{O}-\text{C})_{\text{AC}}$ bonds should not be excluded as well. The $(\text{H}-\text{C})_{\text{PHS}}$ component abbreviates the H–C bonds in the aromatic ring, while $(\text{O}-\text{C})_{\text{AC}}$ one – AC surface. The existence of $(\text{H}-\text{C})_{\text{PHS}}\cdots(\text{O}-\text{C})_{\text{AC}}$ surface interactions can explain notably lower intensity of the H–C bands in the infrared spectra of xPHS/AC in comparison with the intensity of the same bands in pure PHS. It worth noted that the intensity of the band at 1113 cm^{-1} in the infrared profile of 66PHS/AC is remarkably less pronounced in comparison with that in the case of 8PHS/AC, 17PHS/AC and 33PHS/AC. This could be attributed to the presence of a great amount of agglomerated PHS particles on the AC surface for 66PHS/AC, which hinders the FT-IR detection [64–66]. Analyzing the vibrational modes in the infrared region above 3400 cm^{-1} , it is seen that the peak due O–H vibrations in xPHS/AC slightly increases in comparison with the FT-IR profile of AC. It shows the presence of: (i) additional O–H groups on the AC surface in the form of $[\text{HSO}_4]^-$ fragments and/or (ii) surface hydrogen bonds with participation of the aromatic ring, namely $(\text{N}-\text{H})_{\text{PHS}}\cdots(\text{O}-\text{C})_{\text{AC}}$ and $(\text{C}-\text{H})_{\text{PHS}}\cdots(\text{O}-\text{C})_{\text{AC}}$.

In summary, the infrared bands registered in bulk PHS and AC do not change its position after the xPHS/AC samples synthesis which allows the surface PHS–AC interactions (identified as $(\text{H}-\text{N})_{\text{PHS}}\cdots(\text{C}-\text{C})_{\text{AC}}$, $(\text{S}-\text{O})_{\text{PHS}}\cdots(\text{C}-\text{C})_{\text{AC}}$ and $(\text{H}-\text{C})_{\text{PHS}}\cdots(\text{O}-\text{C})_{\text{AC}}$) to be referred as primary electrostatic in nature.

3.2.2. Core-electron levels description

To confirm the FT-IR results, XPS analysis of AC and xPHS/AC systems is conducted. XPS of O 1 s and C 1 s core-electron levels for activated carbon, and O 1 s, C 1 s, N 1 s and S 2p lines for heterogenized ionic liquid are illustrated in Fig. 4. The surface atomic concentrations of the elements in the studied samples are depicted in Table 2.

Results exposed that components with binding energy (BE) values of 285.0, 286.2, 287.9, 290.4 and 292.6 eV present in the C 1 s spectrum of non-modified AC. The first of them describes sp^3 bulk bonded carbon (C–C) in graphite structure [67], while the second one (286.2 eV) is recognized as C–O chemical bonds [68]. In light of this, the components with BE values of 287.9 and 290.4 eV are due to C = O [69] and O–C = O [70] groups, respectively. The component with the highest binding energy (292.6 eV) is referred as a shake-up satellite peak due to $\pi \rightarrow \pi$ conjugation [71]. Studying the XPS O 1 s line of AC, the presence of above noted functional groups on the support surface is undoubtedly confirmed. In details, components at 531.7 (C = O) [69], 533.5 (C–O) [51] and 535.6 eV (O–C = O) [72] are detected. C 1 s and O 1 s effects for AC completely coincide with the corresponding phase composition analysis (Fig. 1A) and FT-IR spectrum (Fig. 3), where: (i) a peak at $2\theta = 26.5^\circ$ due to crystal graphite and (ii) infrared bands (within 1000 – 1120 and 1722 cm^{-1}) related to different types of surface oxygen-containing species are registered.

It is established that the sp^3 bulk bonded carbon (53 at.%) is the most pronounced component in the XPS spectrum of AC, followed by the C 1 s components at 286.2 (20 at.%), 287.9 (9 at.%), 290.4 (8

at.%) and 292.6 eV (5 at.%). In light of this, contributions values of 1.5, 2.5 and 0.7 are established to characterize the O 1 s components at 531.7, 533.5 and 535.6 eV, respectively. Based on the above, carbon and oxygen concentrations of 95 and 5 at.%, respectively denote the activated carbon surface. Notably lower contribution of surface oxygen in comparison with the surface carbon in the XPS spectrum of AC agrees well with FT-IR profile of the carrier, where the presence of surface oxygen-containing species is presented as bands of low intensity.

Impregnation of the activated carbon carrier with small amounts (8 wt%) of pyridinium hydrogen sulfate slightly decreases/increases the surface carbon/oxygen concentration on AC to 92/7 at.%, which could be attributed to a poorly covered AC surface by ionic liquid particles. It is in accordance with the FT-IR data, where the PHS phase on AC surface is presented as infrared peaks of low-intensity. XPS C 1 s line of 8PHS/AC sample revealed components at 285.0, 286.0 and 287.6 eV, which do not differ (as contribution and position) from those (285.0, 286.2 and 287.9 eV) observed previously for AC. Hence, it is reasonable to assume that the components within 285–288 eV in the in the XPS spectrum of 8PHS/AC describe the support surface. It is interesting to point out that the component at 290.4 eV in the C 1 s spectrum of AC is characterizes with a notably lower BE value (289.5 eV) when 8PHS/AC is obtained. This could be correlated to the presence of a reductive atmosphere in the form of C–H and N–H fragments in pyridine ring. As a result, hydrogen bonds such as $(\text{N}-\text{H})_{\text{PHS}}\cdots(\text{O}-\text{C})_{\text{AC}}$ and $(\text{C}-\text{H})_{\text{PHS}}\cdots(\text{O}-\text{C})_{\text{AC}}$ are present on the carrier surface, being already proposed by FT-IR analysis. However, this component can be interpreted as carbon attached to a less electronegative atom such as hydrogen in the environment of nitrogen one. In other words, the component at 289.5 eV in the C 1 s spectrum of 8PHS/AC may describe the aromatic H–C–N bonds in the PHS structure. The existence of PHS particles on the AC surface is confirmed when the highest binding energy components (shake-up satellite peak due to $\pi \rightarrow \pi$ conjugation) in the C 1 s line of AC and 8PHS/AC samples are studied. It is revealed that the AC impregnation with PHS ionic liquid causes BE variety from 292.6 (AC) to 291.6 eV (8PHS/AC), which corresponds to a change in the activated carbon structure after PHS immobilization. The latter agrees well with the XRD data, where a reduced graphite crystallites size due to a surface PHS–AC interaction is observed.

Comparing the O 1 s lines of AC and 8PHS/AC samples, it is found that the components at 531.7, 533.5 eV in AC spectrum raised with 50 and 17 %, respectively after PHS deposition. It suggests that additional amounts of C = O and O–C fragments (consequence of surface PHS–AC interaction) on the AC surface in the presence of PHS are formed, supporting the FT-IR data. On the other hand, components with BE values of 531.7 and 533.5 eV are found to characterize oxygen in the form of HSO_4^- [73,74] and SO_4^{2-} [65,75] groups. Hence, notably promoted participation of the components at 531.7 and 533.5 eV in the O 1 s line of 8PHS/AC system is mainly attributed to oxygen in the heterogenized ionic liquid. Similar to the components between 531 and 534 eV in O 1 s line of AC, the contribution of this at 535.6 eV is discovered to increase notably (30%) in the case of 8PHS/AC as well. Moreover, its BE shifts from 535.6 (AC) to 536.4 eV (8PHS/AC). These observations propose that a large amount of weakly bonded oxygen-containing species (such as O–H groups) populate the 8PHS/AC surface.

An indication for the presence of PHS phase on the AC surface is also obtained evaluating the S 2p and N 1 s core-electron levels (Fig. 4, Table 2). The S 2p line of 8PHS/AC showed two characteristic doublets at BE values of 169.9 (S $2p_{1/2}$) and 168.8 eV (S $2p_{3/2}$), which are typical for SO_4^{2-} groups [76]. In this regard, the N 1 s core-electron level of 8PHS/AC is presented as a single peak at

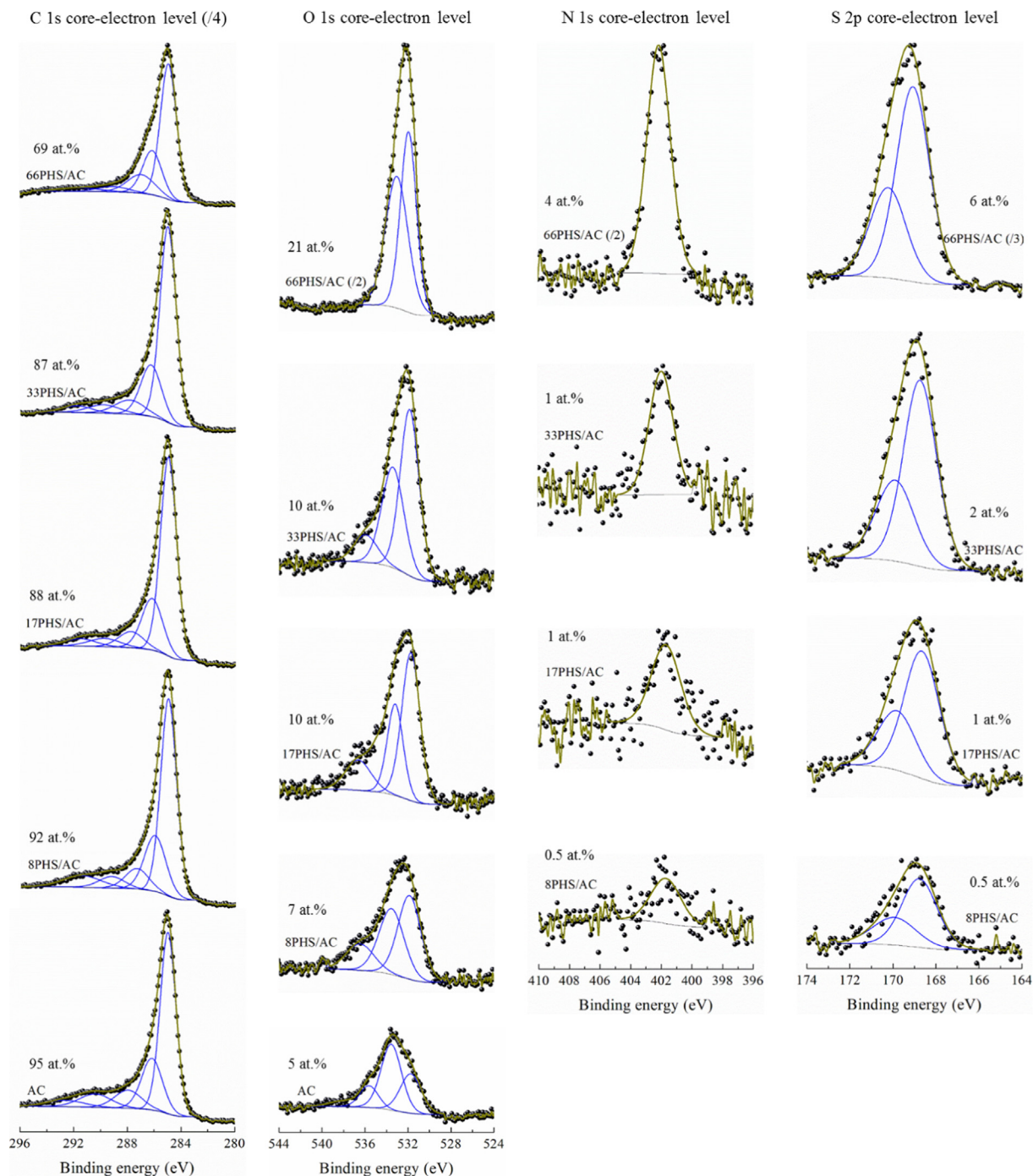


Fig. 4. XPS core-electron levels for AC and xPHS/AC samples.

401.7 eV due to a protonated nitrogen atom (as C–N⁺ and/or N–H⁺) in the PHS structure. Almost identical results are reported for the ionic liquid [C₈C₁Im]⁺[Tf₂N][–], where the nitrogen atom in the imidazolium ring is detected as a signal at 401.9 eV in the N 1s spectrum [77]. In another work, binding energy shifts for nitrogen-containing graphene-based catalysts are studied [78]. The authors established the presence of a quaternary nitrogen atom (C–N⁺) as a peak appeared at 401.8 eV in the N 1s line of the samples.

Results showed that the AC impregnation with moderated amounts (17, 33 and 66 wt%) of pyridinium hydrogen sulfate leads to a surface lower carbon concentration on the 17PHS/AC (88 at.%) 33PHS/AC (87 at.%) and 66PHS/AC (69 at.%) in comparison with

that (92 at.%) registered for 8PHS/AC sample. The latter is interpreted as a more covered AC surface by PHS particles in the case of 17PHS/AC, 33PHS/AC and 66PHS/AC than 8PHS/AC. This statement is confirmed by a higher surface oxygen concentration registered on 17PHS/AC (10 at.%), 33PHS/AC (10 at.%) and 66PHS/AC (21 at.%) with respect to that (7 at.%) on 8PHS/AC. Considering that the surface carbon and oxygen concentrations on 17PHS/AC do not differ from the respective ones on 33PHS/AC, a very similar PHS rearrangement on the 17PHS/AC and 33PHS/AC surfaces is expected. The latter is in accordance with the XRD (Table 1) and FT-IR (Fig. 3) analyses where: (i) values of 7.6 and 7.8 nm are determined as a PHS particles size for 17PHS/AC and 33PHS/AC, respectively

Table 2
XPS core-electron levels and atomic concentrations for AC and xPHS/AC samples.

Core level	Samples				
C1s (eV)	AC	8PHS/AC	17PHS/AC	33PHS/AC	66PHS/AC
	285.0 (53)*	285.0 (51)	285.0 (55)	285.0 (55)	285.0 (39)
	286.2 (20)	286.0 (20)	286.2 (18)	286.3 (18)	286.2 (15)
	287.9 (9)	287.6 (8)	287.8 (7)	287.9 (7)	287.0 (9)
	290.4 (8)	289.5 (5)	289.7 (4)	289.8 (4)	289.1 (3)
O1s (eV)	292.6 (5)	291.6 (7)	291.5 (4)	291.8 (3)	291.6 (3)
	531.7 (1.5)	531.8 (3)	531.8 (5)	531.8 (5)	532.0 (10)
	533.5 (2.5)	533.5 (3)	533.6 (3)	533.7 (4)	533.1 (11)
	535.6 (0.7)	536.4 (1)	536.5 (1)	536.2 (1)	–
N1s (eV)	–	401.7 (0.5)	401.7 (1)	402.0 (1)	402.1 (4)
S2p _{3/2} (eV)	–	168.8 (0.5)	168.7 (1)	168.8 (2)	169.1 (6)

* Component contribution (at.%)

and (ii) absorption bands of comparable intensity are detected in the infrared spectra of 17PHS/AC and 33PHS/AC. Notably more pronounced oxygen concentration on the 66PHS/AC surface in comparison with that on 8PHS/AC, 17PHS/AC and 33PHS/AC is attributed to the higher PHS content used for 66PHS/AC sample preparation.

A detailed XPS study of the 8PHS/AC, 17PHS/AC and 33PHS/AC systems exposed that the ionic liquid content does not affect the binding energy (position) of the components in C 1 s, O 1 s, S 2p and N 1 s lines. It implies that similar surface effects characterize 8PHS/AC, 17PHS/AC and 33PHS/AC systems. However, the BE of the components at 287.0 and 289.1 eV in the C 1 s spectrum of 66PHS/AC is lower than those registered for 8PHS/AC (287.6 and 289.5 eV), 17PHS/AC (287.8 and 289.7 eV) and 33PHS/AC (287.9 and 289.8 eV). This could be related to an increased reductive atmosphere (such as C–H and N–H moieties in aromatic ring) on the AC surface, a consequence of the increased ionic liquid loading. As expected, the components in S 2p (SO₄²⁻) and N 1 s (H–N⁺) spectra of 17PHS/AC, 33PHS/AC and 66PHS/AC enlarge with the ionic liquid content in accordance with XRD, S_{BET} and FT-IR studies. Indeed, the surface PHS population is established to increase in order 8PHS/AC < 17PHS/AC < 33PHS/AC < 66PHS/AC.

It was noted above that the surface carbon concentration decreases with rising the PHS content and these effect was correlated to a moderated number of PHS particles covering the support surface. However, the ionic liquid applied in this work contains a significant amount of carbon atoms (in the form of [H–Pyr]⁺), i.e. the surface carbon concentration on the 8PHS/AC, 17PHS/AC, 33PHS/AC and 66PHS/AC samples should increase (as the oxygen concentration does). To avoid this discrepancy, it is assumed that the cationic moiety is mainly involved in the surface PHS–AC interaction during heterogenization. As a result, the PHS species are oriented perpendicularly to the support surface and the oxygen-containing fragment in the ionic liquid, namely [HSO₄]⁻, is predominantly recorded by XPS. This statement agrees with the FT-IR data spectra of xPHS/AC samples, where bands due to C–H and N–H vibrational modes in [H–Pyr]⁺ are hard to be observed. At the same time, the infrared peaks related to S–O vibrations in the [HSO₄]⁻ moiety become more noticed with increasing the PHS content.

3.3. Catalytic performance

The catalytic activity of PHS heterogenized on AC is evaluated in a process of butyl acetate synthesis at reaction temperature of 80 °C, initial reactants molar ratio of unit and a catalyst loading of 10 wt% (Fig. 5). For comparison, the butyl acetate yield for the non-catalyzed (blank) reaction is also added.

Results showed that the acetic acid esterification without a catalyst leads to an ester yield of 4.91 % after 90 min reaction time. In other words, synthesis of butyl acetate practically does not occur

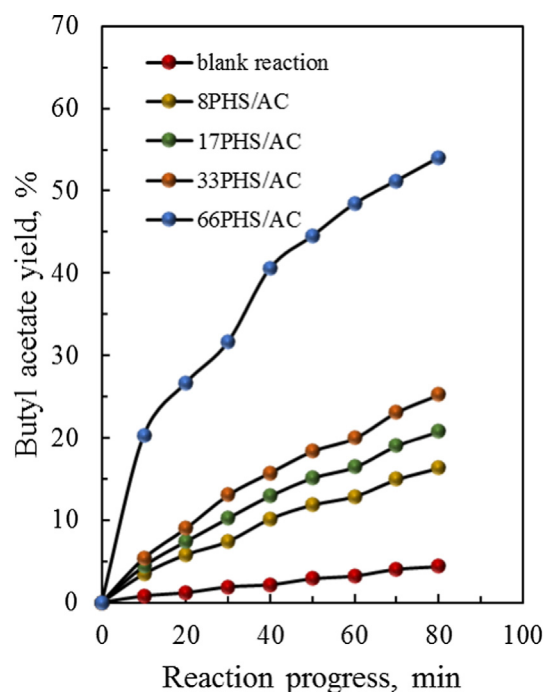


Fig. 5. Butyl acetate yield in the presence of xPHS/AC. Reaction conditions: 10 wt% catalyst, initial reactants molar ratio of unit, reaction temperature of 80 °C.

in the absence of a catalyst. However, the addition of 8PHS/AC, 17PHS/AC, 33PHS/AC and 66PHS/AC catalyst causes the ester yield to increase notably up to 18.66, 23.00, 27.34 and 56.63%, respectively. The latter is found to be notably higher than that (40.55%) registered in the butyl acetate synthesis using tris(2-amino-1,3-thiazolium) hydrogen sulfate sulfate monohydrate immobilized on α -Al₂O₃ [79]. In another work rice husk ash supported pyridinium hydrogen sulfate gerates a butyl acetate yield of 51.20% [20].

Variety of the ester yield in the presence of xPHS/AC catalysts is connected with the fact that the activation of a carboxylic acid (such as acetic acid) during esterification proceeds via protonation of carbonyl oxygen, a consequence of a proton (H⁺) transfer from the acidic catalyst toward the substrate [79–82]. As a result, an active complex due to a carboxylic acid-catalyst interaction is formed. On the other hand, the greater the number of active complexes, the higher the degree of substrate conversion [83]. Hence, the presence of a greater number of active complexes on the support surface can explain superior butyl acetate yield in the presence of xPHS/AC systems. Moreover, the latter may explain the increasing of acetic acid conversion with rising the PHS content

as well. It is in accordance with the XRD, FT-IR and XPS data which undoubtedly exposed that the amount of surface PHS particles increases in order 8PHS/AC < 17PHS/AC < 33PHS/AC < 66PHS/AC. Similar catalytic performance of 17PHS/AC and 33PHS/AC samples correlates with the almost identical size (Fig. 1, Table 1) and population (Figs. 3 and 4, Table 1) of PHS particles on their surfaces.

It was established earlier (see pt. 3.1.) that the PHS particles size on the AC surface increases as follows: 8PHS/AC (6.3 nm) < 17PHS/AC (7.6 nm) \approx 33PHS/AC (7.8 nm) < 66PHS/AC (14 nm). At first sight, it assumes that a notable PHS moiety on the 66PHS/AC surface will not be available for substrate activation, i.e. the ester yield in the case of 66PHS/AC catalyst is expected to be lower than that for 8PHS/AC, 17PHS/AC and 33PHS/AC. However, FT-IR and XPS measurements established that the surface PHS-AC interaction for all of the xPHS/AC catalysts is primary electrostatic in nature and it does not depend on the PHS content applied for AC impregnation. Hence, the catalytic activity of xPHS/AC is affected by the surface active phase amount, but not the PHS particle size. Since 66PHS/AC sample possesses the highest catalytic activity, it is preferred as a catalyst for further thermodynamic (equilibrium constant, reaction enthalpy and entropy) and kinetic (influence of the catalyst loading reaction and temperature) studies.

3.4. Recycling of the heterogenized PHS ionic liquid

The feasibility and sustainable development of any catalytic process depends on the reusability of the catalyst. One of the primary aims of this study is to investigate the recycling of heterogenized PHS ionic liquid (66PHS/AC). Since the 66PHS/AC sample is in a solid state (a heterogeneous catalyst), it can be separated from the liquid reaction mixture by decantation. Separated 66PHS/AC catalyst is then regenerated by vaporization in vacuum (0.005 MPa) at 90 °C for 1.0 h to ensure that there are no other chemical residues in the sample to affect the calculation of catalyst recovery. The catalyst recycle results are shown in Table 3. It is found that five cycles have been successively completed and no obvious change is observed on the recovered catalytic activity and quantity. The slight decrease in the yield of butyl acetate is ascribed to the slight loss of exposed surface PHS phase due to the transferring of samples during the regeneration.

3.5. Equilibrium constant, reaction enthalpy and entropy

Considering that the esterification process is a reversible reaction, the substrate conversion is highly affected by the chemical equilibrium, even at a large alcohol-to-acid molar ratio [84]. Hence, equilibrium constant (expresses the composition of a system at equilibrium) needs to be known.

Based on the equilibrium reactants concentrations, the equilibrium constant (K_C) values for the reaction of butyl acetate production at different reaction temperatures are obtained (Eq. (3)).

Table 3
Recycling of 66PHS/AC catalyst for butyl acetate synthesis.^a

Run	Ester yield, %	Catalyst weight at each run, g	Cumulative recovery of catalyst, %
1	56	2.50	100
2	55	2.48	99.2
3	54	2.41	96.5
4	54	2.38	95.1
5	53	2.37	94.8

^a Reaction conditions: acetic acid 0.4161 mol; butanol 0.4161 mol; 10 wt% catalyst with respect to the mass of acetic acid; reaction temperature 80 °C; reaction time 90 min.

$$K_C = \frac{k_1}{k_2} = \frac{C_{B_e} C_{Z_e}}{C_{A_e} C_{Y_e}} = \frac{X_{A_e}^2}{(1 - X_{A_e})^2} \quad (3)$$

where, k_1 and k_2 are forward and backward rate constants, respectively (l/mol \times min); C_{i_e} ($i \equiv A, Y, B, Z$) corresponds to equilibrium concentration (mol/l) of acetic acid, butanol, butyl acetate and water; X_{A_e} abbreviates the acetic acid conversion at equilibrium conditions.

It is revealed that K_C increases with the reaction temperature rising, which means that the biodiesel synthesis is an endothermic process. In details, values of 3.778, 4.621, 5.232, 6.208 and 7.295 are exposed as K_C at reaction temperature of 40, 50, 60, 70 and 80 °C, respectively (Table 4). The K_C values registered in this paper correlate well with the generally accepted statement that the equilibrium constant of esterification reactions have values within 1–10 [85]. Vojtko and co-authors [86] and Sarlo et al. [87] analyzed the esterification of secondary alkan-2-ols with acetic acid at 60 °C using H_2SO_4 as a catalyst and reported for K_C values between 0.23 and 3.85. In another work, a kinetic study of the esterification of lactic acid by ethanol at 70, 75 and 80 °C in the presence of Preissler acid exposed equilibrium constant of 0.044, 0.053 and 0.055, respectively [88]. Temperature dependence of the equilibrium constant, expressed by means of the classical relation of van't Hoff (Eq. (4)), allows enthalpy and entropy of a reaction to be determined.

$$\ln K_C = \left(-\frac{\Delta H_r^\circ}{RT} \right) + \left(\frac{\Delta S_r^\circ}{R} \right) \quad (4)$$

where, ΔH_r° (kJ/mol) is the standard enthalpy change of a reaction and ΔS_r° (J/mol \times K) is the change in entropy of the reaction system.

Standard enthalpy represents the amount of absorbed/released heat in a reaction, i.e. it indicates whether a reaction is endothermic/exothermic in nature. A plot of the equilibrium constant ($\ln K_C$) as a function of the reaction temperature ($1/T$) is given in Fig. 6. As can be seen, a line with a negative slope of $(-\Delta H_r^\circ/R)$ and an intercept of $(\Delta S_r^\circ/R)$ is obtained. The negative slope confirms that the reaction of butyl acetate synthesis is endothermic in nature, being revealed by K_C increasing with the reaction temperature. Based on Eq. (4), ΔS_r° and ΔH_r° for the butyl acetate synthesis in the presence of 66PHS/AC catalyst are calculated as 59.69 J/mol \times K and 15.26 kJ/mol, respectively. The positive ΔS_r° value is another indication that the increasing of reaction temperature favors the reaction of butyl acetate synthesis.

Knowing ΔH_r° and ΔS_r° values, Gibbs free energy (ΔG_r°) at different reaction temperature is found by means of the relation $\Delta G_r^\circ = \Delta H_r^\circ - T\Delta S_r^\circ$. Thus, values of -3.423, -4.019, -4.617, -5.214 and -5.811 kJ/mol characterize ΔG_r° for the reaction of butyl acetate synthesis at 40, 50, 60, 70 and 80 °C, respectively. Analyzing ΔG_r° as a function of the reaction temperature, an inverse trend is observed, namely the ΔG_r° values reduce with the temperature increasing. Considering that reacting systems are characterized with a minimum of the Gibbs free energy [89], the ΔG_r° diminishing with reaction temperature rising is another conformation that elevated temperatures favors the butyl acetate production.

3.6. Influence of the catalyst loading

In the previous subsection was noted that the rate determine step in a catalyzed esterification process is a substrate-catalyst interaction, which leads to formation of an active complex (a protonated form of the substrate). Since a high value described the substrate concentration at the start of the esterification reaction, a great number of active complexes should be expected as well.

Table 4
Kinetic and thermodynamic parameters for butyl acetate synthesis using 66PHS/AC.

Temperature ^a	Reaction rate constants (l/mol × min)		K _C	X _{Ae}	ΔGr°/kJ/mol	ΔGr [‡] /kJ/mol
	k ₁ × 10 ⁻⁴	k ₂ × 10 ⁻⁴				
40 °C	6.12 ± 0.23	1.62 ± 0.09	3.778	0.6603	-3.423	96.36
50 °C	7.76 ± 0.43	1.68 ± 0.12	4.621	0.6825	-4.019	99.43
60 °C	9.65 ± 0.75	1.84 ± 0.18	5.231	0.6958	-4.617	102.51
70 °C	15.45 ± 0.96	2.49 ± 0.19	6.208	0.7136	-5.214	105.59
80 °C	24.32 ± 1.16	3.29 ± 0.26	7.295	0.7298	-5.811	108.69
Catalyst loading ^b						
5 wt%	12.15 ± 0.77	1.62 ± 0.24				
10 wt%	24.32 ± 1.16	3.29 ± 0.26				
12 wt%	28.95 ± 1.22	3.61 ± 0.31				
15 wt%	30.98 ± 1.25	4.13 ± 0.33				

^a Reaction conditions: 10 wt% catalyst; initial reactants molar ratio of unit; reaction time 90 min.

^b Reaction conditions: initial reactants molar ratio of unit; reaction time 90 min; reaction temperature 80 °C.

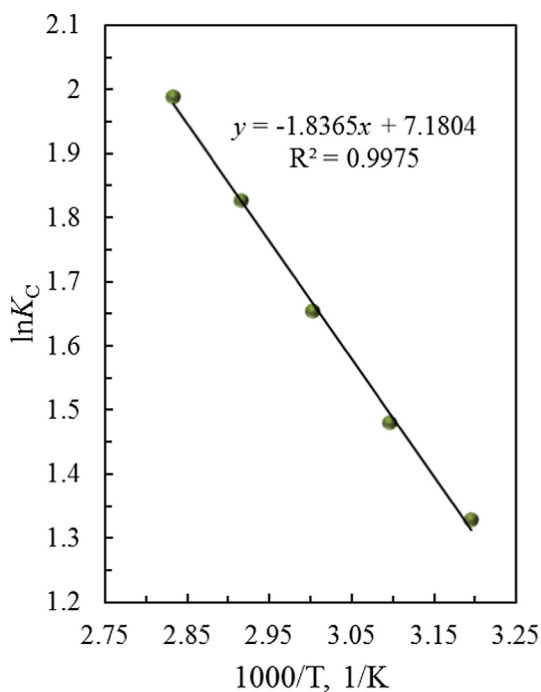


Fig. 6. Van't Hoff plot for finding the enthalpy and entropy of butyl acetate synthesis. Reaction conditions: 10 wt% 66PHS/AC catalyst, initial reactants molar ratio of unit, 90 min reaction time.

However, the substrate concentration decreases during reaction progress, which overturns the active complex formation and the catalyst loading (L_{cat}) becomes poorer. Thus, to increase the overall reactants conversion, L_{cat} plays a major role. Effect of L_{cat} (5–15 wt%) on the butyl acetate yield is investigated at reaction temperature of 80 °C and initial reactants molar ratio of unit (Fig. 7A). Blank reaction of butyl acetate synthesis is added for comparison.

Results revealed that the usage of small amounts (5 wt%) of 66PHS/AC catalyst improves the acetic acid esterification, being observed by remarkably increased butyl acetate yield from 4.91 (blank reaction) to 40.95%. It is found that the 66PHS/AC amount increasing up to 10 wt% promotes the reaction of acetic acid esterification, where a value of 56.63% is registered as an ester yield. However, further L_{cat} rising up to 12 and 15 wt% favors insufficiently butyl acetate synthesis, since ester yields of 59.37 and 62.12% are reached, respectively. Taking into account that the catalyst loading within 12–15 wt% slightly changes the main product yield, a value of 12 wt% can be referred as an optimal 66PHS/AC content. Improved butyl acetate production when L_{cat} increases is

related to the formation of a greater number of active carbonyl complexes (more species of protonated substrate). This statement correlates well with a work of Wanchoo and co-authors [90], where methylation of propylacetic acid is investigated at 60 °C in the presence of Amberlyst 15 catalyst. A notably promoted carboxylic acid conversion is registered when the catalyst loading varies within 32.87–65.80 g/l due to an enhanced number of H^+ ions, available for substrate activation.

Findings that: (i) the presence of a catalyst favors the butyl acetate production and (ii) 12 wt% is an optimal 66PHS/AC loading are confirmed by the calculated forward rate constant. For that purpose, the following kinetic model is applied:

$$\frac{X_{Ae}^2}{(2 - 2X_{Ae}^2)C_{A0}} \ln \left[\frac{X_{Ae} - (2X_{Ae} - 1)X_A}{X_{Ae} - X_A} \right] \equiv Y = k_1 t \quad (5)$$

Plotting Y as a function of the reaction time (t), a straight line passing through origin is occurred. The slope of the line represents the forward rate constant value. Based on the Eq. (5), k_1 value of 12.15×10^{-4} l/mol × min is obtained for the reaction of butyl acetate synthesis in the presence of 5 wt% 66PHS/AC, which is more than 13 times higher than k_1 (0.88×10^{-4} l/mol × min) for the blank reaction (Fig. 7B, Table 4). In this regard, the rate constant (24.32×10^{-4} l/mol × min) for butyl acetate production using L_{cat} of 10 wt% is higher than that of the process conducted with $L_{cat} = 5$ wt%. In accordance with the similar butyl acetate yields reached in the presence of 12 and 15 wt% 66PHS/AC, values of 28.95 and 30.98×10^{-4} l/mol × min are evaluated as a forward rate constant, respectively.

3.7. Influence of the reaction temperature

Effect of the reaction temperature on the butyl acetate yield (Fig. 8A) and forward rate constant (Fig. 8B) is investigated in the temperature interval within 40–80 °C, initial reactants molar ratio of unit and 10 wt% 66PHS/AC catalyst.

Results exposed that values of 26.41% and 6.12×10^{-4} l/mol × min characterize butyl acetate yield and forward rate constant at 40 °C, respectively. It is found that increasing the reaction temperature up to 50, 60, 70 and 80 °C promotes the butyl acetate production, since values of 31.55, 36.69, 46.66 and 56.63% are registered as an ester yield, respectively. In addition, the forward rate constants are determined as 7.76 (50 °C), 9.65 (60 °C), 15.45 (70 °C) and 24.32 (80 °C) × 10^{-4} l/mol × min (Table 4). Applying Eq. (3), the respective backward rate constants (k_2) at 40, 50, 60, 70 and 80 °C can be easily calculated. Superior butyl acetate yield and rate constants (k_1 and k_2) at high temperature is related to the fact that the elevated temperature helps the reactant molecules to obtain adequate energy to cross the energy bar-

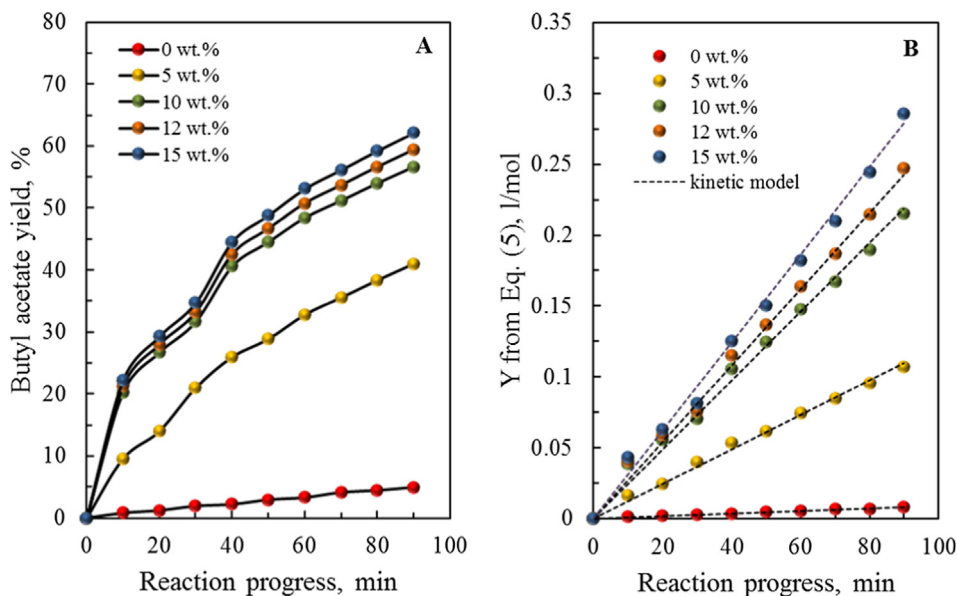


Fig. 7. Influence of the 66PHS/AC loading on the butyl acetate yield (A) and forward rate constant (B). Reaction conditions: reaction temperature of 80 °C and initial reactants molar ratio of unit.

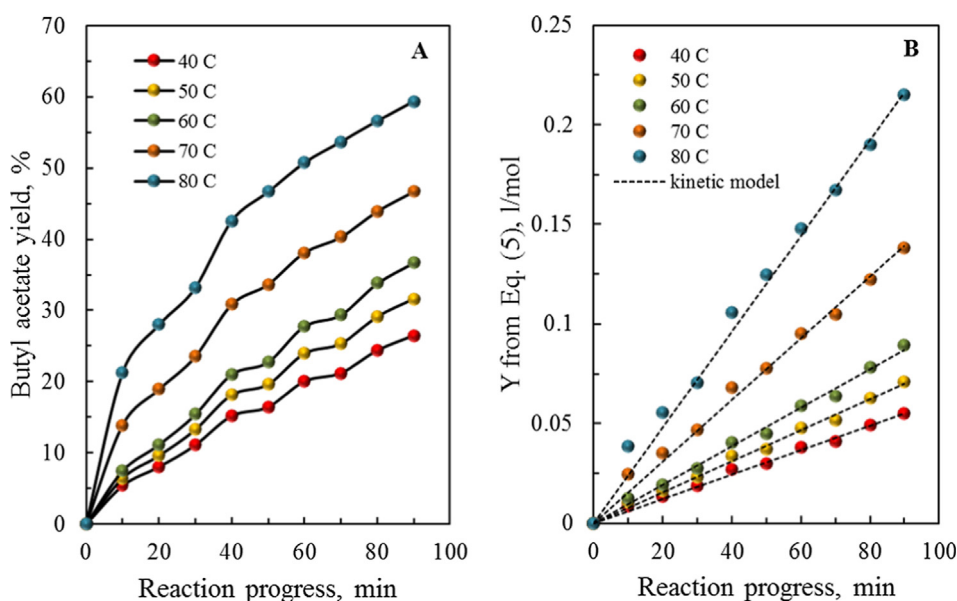


Fig. 8. Influence of the reaction temperature on the butyl acetate yield (A) and forward rate constant (B). Reaction conditions: 10 wt% 66PHS/AC and initial reactants molar ratio of unit.

rier [91]. In this sense, the reaction of butyl acetate synthesis is endothermic in nature, as it was noted earlier (see *pt.* 3.4.).

Although the butyl acetate synthesis is denoted as an endothermic reaction in the present work, quite different point of views about the temperature influence on the reactants conversion (equilibrium constant) in terms of esterification are present in the literature. For example, the kinetics of acetic acid methylation in the presence of Indion 130 and showed K_C values of 5.009, 6.521 and 9.265 at temperature of 60, 70 and 80 °C, respectively [92]. Based on these, the authors classify the methyl acetate production as an endothermic reaction, as it was stated in the current work for butyl acetate synthesis. Unlike Saidutta et al. [92] and the data presented in the current paper, Tao et al. [14] denoted the reaction of butyl acetate synthesis as exothermic in nature since the rise in temperature from 60 to 80 °C diminishes K_C from 13.931 to 12.947. In

other words, the increase in temperature shifts the system in the backward direction to alleviate the stress of additional heat. However, in the same work [14] reported that the rise in temperature improves the acetic acid conversion toward ester. Accordingly, their statement that K_C decreases with the temperature rising seems very speculative. The lack of consensus about the temperature dependence of K_C in terms of esterification reaction is confirmed by the work of Akyalçın and Altıokka [93], where octyl acetate synthesis in the presence of Amberlyst 36 is conducted. An equilibrium constant (60.7) which is independent of temperature within 60–80 °C is reported in that case. Temperature independence of K_C is noted in the case of heterogeneously-catalyzed esterification of succinic acid with ethanol as well [94].

When the forward and backward rate constants at different reaction temperatures are known, the activation energy and pre-

exponential factor for the forward (butyl acetate synthesis) and backward (butyl acetate hydrolysis) reactions in the presence of 66PHS/AC catalytic system are calculated via Arrhenius's law:

$$\ln k = \ln A - \frac{E_A}{RT} \quad (6)$$

where, E_A is activation energy (kJ/mol), A is pre-exponential factor (l/mol \times min), R is gas constant (8.314 J/mol \times K) and T is absolute temperature (K).

Plotting $\ln k$ versus $1/T$ (Fig. 9A), values of 31.53 and 16.51 kJ/mol are calculated as activation energies for the forward (E_{A_f}) and backward (E_{A_b}) reactions, respectively. In light of this, A_f and A_b are established to be 10.03 and 0.08×10^6 l/mol \times min, respectively. It is obvious that the activation energy of the forward reaction is about two times higher than that of the backward one, which can be explained as follows. During the course of a given reaction, there exists an intermediate stage (transition state), where chemical bonds are partially broken and partially formed. This transition state is at a higher energy level than the starting reactants and it is very unstable. The energy required to reach this transition state is called activation energy. In the case of an endothermic reaction (such as butyl acetate synthesis), the reactants are at a lower energy level compared to the products. It means that a higher energy (E_A) is required to force the reaction in the forward direction in accordance with the relation $E_{A_f} = E_{A_b} + \Delta H_r^\circ$. Based on the latter, the difference (15.02 kJ/mol) between E_{A_f} and E_{A_b} is found to be identical to the calculated reaction enthalpy (ΔH_r°), namely 15.26 kJ/mol. Since the pre-exponential factor expresses the number of effective impacts between reactants in a chemical process, the remarkably higher A_f value (10.03×10^6 l/mol \times min) with respect to A_b (0.08×10^6 l/mol \times min) agrees well with notably more favored butyl acetate synthesis than butyl acetate hydrolysis at selected reaction conditions.

Speaking for activation energy and transition state, enthalpy (ΔH^\ddagger) and entropy (ΔS^\ddagger) of activation for the reaction of butyl acetate production are calculated as well (Fig. 9B). For that purpose, the Eyring's equation is used:

$$\ln\left(\frac{k_1}{T}\right) = \ln\left(\frac{k_B}{h}\right) + \frac{\Delta S^\ddagger}{R} - \frac{\Delta H^\ddagger}{RT} \quad (7)$$

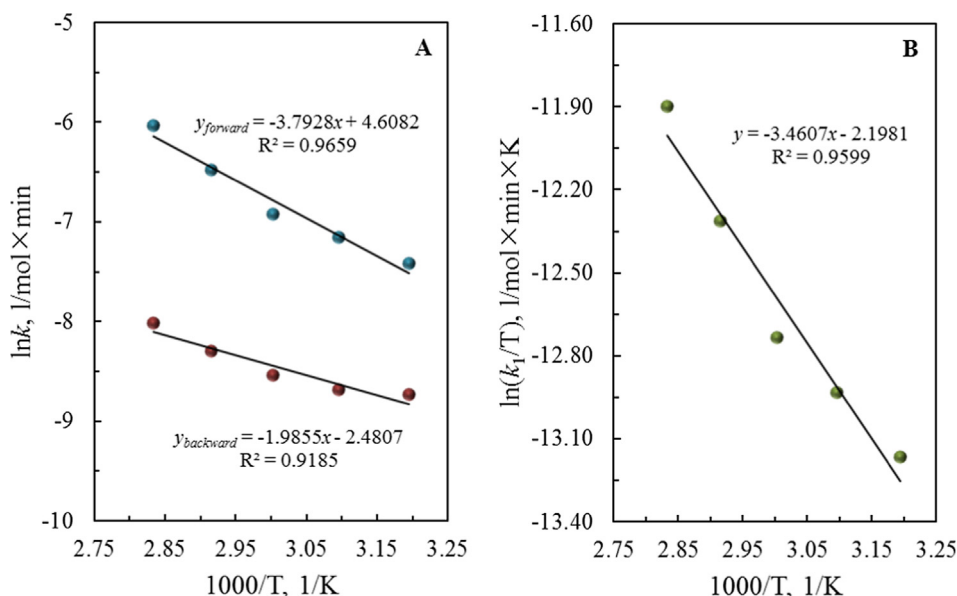


Fig. 9. Arrhenius plot for finding the activation energy and the pre-exponential factor (A) and Eyring plot for finding the entropy and enthalpy of activation (B) of butyl acetate synthesis in the presence of 66PHS/AC catalyst. Reaction conditions: 10 wt% 66PHS/AC catalyst, initial reactants molar ratio of unit, 90 min reaction time.

where, k_B is Boltzmann constant (1.38×10^{-23} J/K), h is Planck constant (6.63×10^{-34} J \times s), ΔH^\ddagger is enthalpy of activation (kJ/mol) and ΔS^\ddagger is entropy of activation (J/mol \times K). If the experimental kinetic data $\ln(k_1/T)$ are plotted versus $(1/T)$, the enthalpy of activation can be calculated from the slope $-(\Delta H^\ddagger/R)$. The corresponding entropy of activation is obtained from the intercept $\ln(k_B/h) + (\Delta S^\ddagger/R)$. Using ΔH^\ddagger and ΔS^\ddagger , the activation energy barrier ($\Delta G^\ddagger = \Delta H^\ddagger - T\Delta S^\ddagger$, kJ/mol) for the process of butyl acetate production is revealed.

Data showed that values of 28.77 kJ/mol and -307.76 J/mol \times K characterize ΔH^\ddagger and ΔS^\ddagger , respectively. It is well known that the ΔS^\ddagger equals the change in entropy when the reactants change from their initial state to the transition state [95]. Thus, ΔS^\ddagger provides clues about the molecularity of the rate determining step in a reaction. Negative ΔS^\ddagger value indicates that entropy decreases on forming the transition state, which shows an associative mechanism in which two reaction partners form a single activated complex. It confirms above statement that the butyl acetate synthesis includes pre-formation of a transition state through a substrate-catalyst interaction.

Based on the ΔH^\ddagger and ΔS^\ddagger values, Gibbs free energy of activation (ΔG^\ddagger) can be easily found. Thus, ΔG^\ddagger at reaction temperature of 40, 50, 60, 70 and 80 $^\circ$ C, ΔG^\ddagger is calculated to be 96.36, 99.43, 102.51, 105.59 and 108.69 kJ/mol, respectively (Table 4). Considering that the bonds cleavage during a chemical reaction requires a certain amount of energy, positive ΔG^\ddagger values are expected. Increased ΔG^\ddagger value with rise of the reaction temperature indicates that elevated temperatures favor the butyl acetate production.

4. Conclusions

Surface effects and textural properties for the new catalytic system xPHS/AC ($x = 8, 17, 33$ and 66 wt%); PHS – pyridinium hydrogen sulfate ionic liquid; AC – activated carbon support) are studied by means N_2 adsorption–desorption measurements, XRD, XPS and FT-IR. Catalytic behavior and recycling of xPHS/AC are investigated in the process of butyl acetate synthesis. Influence of the reaction temperature and catalyst content on the ester yield is also revealed. The thermodynamic functions equilibrium constant, acti-

vation energy, Gibbs free energy and activation energy barrier for the reaction of butyl acetate production in the presence of x PHS/AC are determined.

The specific surface area and the total pore volume decrease with rise in the PHS content during heterogenization due to filling of the support pores with ionic liquid species. These can migrate on AC surface and a PHS particles size order 8PHS/AC < 17PHS/AC \approx 33PHS/AC < 66PHS/AC is noted. On the other hand, surface PHS-AC interactions in the form of $(\text{H}-\text{N})_{\text{PHS}} \cdots (\text{C}-\text{C})_{\text{AC}}$, $(\text{S}-\text{O})_{\text{PHS}} \cdots (\text{C}-\text{C})_{\text{AC}}$ and $(\text{H}-\text{C})_{\text{PHS}} \cdots (\text{O}-\text{C})_{\text{AC}}$ bonds are detected on the AC surface. It is stated that these surface bonds are electrostatic in nature and their strength is independent on the PHS content applied for AC impregnation. Hence, the PHS particles size variety on the AC surface is attributed to the PHS loading, rather than the PHS-AC interaction strength.

Catalytic activity increases in order 8PHS/AC < 17PHS/AC \approx 33PHS/AC < 66PHS/AC, a consequence of a moderated amount of a surface PHS phase. No obvious change on the recovered catalytic activity and quantity after five cycles is observed. Variety of the catalyst loading (L_{cat}) within 5–12 wt% increases the butyl acetate yield and rate constant due to a higher number of active carbonyl complexes. Further L_{cat} increasing up to 12 and 15 wt% does not affect notably the ester yield and rate constant. Rise in the reaction temperature between 40 and 80 °C promotes the butyl acetate production and forward rate constant, since the reactant molecules possess adequate energy to cross the energy barrier. Values of 31.53 kJ/mol and 10.03×10^6 l/mol \times min, 59.69 J/mol \times K and 15.26 kJ/mol are calculated as E_{A} , A_{r} , $\Delta S_{\text{r}}^{\circ}$ and $\Delta H_{\text{r}}^{\circ}$, respectively for the process of butyl acetate synthesis at 80 °C. Moreover, ΔH^{\ddagger} and ΔS^{\ddagger} , $\Delta G_{\text{r}}^{\circ}$, and ΔG^{\ddagger} are found to be 28.77 kJ/mol, -307.76 J/mol \times K, -5.811 kJ/mol and 108.69 kJ/mol, respectively at the same reaction temperature.

CRedit Author Statement

XPS analysis was conducted by Hristo Kolev, associated professor. XRD measurements were conducted by Georgi Avdeev, Senior Assistant Textural, FT-IR and UV-vis data as well as tables and graphs formatting, results interpretation and manuscript writing is conducted by the corresponding author Ivaylo Tankov, Senior Assistant.

Declaration of Competing Interest

The authors declare that they have no known competing financial interests or personal relationships that could have appeared to influence the work reported in this paper.

Appendix A. Supplementary material

Supplementary data to this article can be found online at <https://doi.org/10.1016/j.molliq.2021.117192>.

References

- [1] S. Kazemiabnavi, Z. Zhang, K. Thornton, S. Banerjee, Electrochemical stability window of imidazolium-based ionic liquids as electrolytes for lithium batteries, *J. Phys. Chem. B* 120 (25) (2016) 5691–5702.
- [2] Li. Xu, X. Cui, Y. Zhang, T. Feng, R. Lin, X. Li, H. Jie, Measurement and correlation of electrical conductivity of ionic liquid [EMIM][DCA] in propylene carbonate and γ -butyrolactone, *Electrochim. Acta* 174 (2015) 900–907.
- [3] A. Deshpande, L. Kariyawasam, P. Dutta, S. Banerjee, Enhancement of lithium ion mobility in ionic liquid electrolytes in presence of additives, *J. Phys. Chem. C* 117 (48) (2013) 25343–25351.
- [4] V.V. Chaban, O.V. Prezhdo, Ionic Vapor composition in pyridinium-based ionic liquids, *J. Phys. Chem. B* 120 (20) (2016) 4661–4667.
- [5] T.L. Greaves, C.J. Drummond, Protic ionic liquids: evolving structure-property relationships and expanding applications, *Chem. Rev.* 115 (20) (2015) 11379–11448.
- [6] I. Tankov, R. Yankova, M. Mitkova, D. Stratiev, Non-isothermal decomposition kinetics of pyridinium nitrate under nitrogen atmosphere, *Thermochim. Acta* 665 (2018) 85–91.
- [7] W.-Q. Feng, Y.-H. Lu, Y. Chen, Y.-W. Lu, T. Yang, Thermal stability of imidazolium-based ionic liquids investigated by TG and FTIR techniques, *J. Therm. Anal. Calorim.* 125 (1) (2016) 143–154.
- [8] M. Raicopol, C. Dascalu, C. Devan, A.L. Alexe-Ionescu, G. Barbero, A simple model of ac hopping surface conductivity in ionic liquids, *Electrochim. Commun.* 100 (2019) 16–19.
- [9] A. Ying, Z. Li, Y. Ni, S. Xu, H. Hou, H. Hu, Novel multiple-acidic ionic liquids: green and efficient catalysts for the synthesis of bis-indolylmethanes under solvent-free conditions, *J. Ind. Eng. Chem.* 24 (2015) 127–131.
- [10] S.P.M. Ventura, F.A. Silva, M.V. Quental, D. Mondal, M.G. Freire, J.A.P. Coutinho, Ionic-liquid-mediated extraction and separation processes for bioactive compounds: past, present, and future trends, *Chem. Rev.* 117 (10) (2017) 6984–7052.
- [11] R. Hayes, G.G. Warr, R. Atkin, Structure and nanostructure in ionic liquids, *Chem. Rev.* 115 (13) (2015) 6357–6426.
- [12] S. Mohammadi, M. Abbasi, Design of ionic liquid sulfonic acid pyridinium hydrogen sulfate as an efficient, eco-friendly, and reusable catalyst for one-pot synthesis of highly functionalized tetrahydropyridines, *Res. Chem. Intermed.* 41 (11) (2015) 8877–8890.
- [13] J. Lunagariya, A. Dhar, R.L. Vekariya, Efficient esterification of *n*-butanol with acetic acid catalyzed by the Brønsted acidic ionic liquids: influence of acidity, *RSC Adv.* 7 (2017) 5412–5420.
- [14] D.-J. Tao, Y.-T. Wu, Z. Zhou, J. Geng, X.-B. Hu, Z.-B. Zhang, Kinetics for the esterification reaction of *n*-butanol with acetic acid catalyzed by noncorrosive Brønsted acidic ionic liquids, *Ind. Eng. Chem. Res.* 50 (4) (2011) 1989–1996.
- [15] L. Reinert, K. Batouche, J.-M. Lévêque, F. Muller, J.-M. Bény, B. Kebabi, L. Duclaux, Adsorption of imidazolium and pyridinium ionic liquids onto montmorillonite: Characterization and thermodynamic calculations, *Chem. Eng. J.* 209 (2012) 13–19.
- [16] Y. He, Q. Zhang, X. Zhan, D.-G. Cheng, F. Chen, Synthesis of efficient SBA-15 immobilized ionic liquid catalyst and its performance for Friedel-Crafts reaction, *Catal. Today* 276 (2016) 112–120.
- [17] J. Safaei-Ghomi, S. Zahedia, H. Basharnavaz, Synthesis and characterization of ionic liquid supported on Fe₂O₃ nanoparticles and a DFT study of 1,3-dipolar cycloaddition for the synthesis of isoxazolidines in the presence of ionic liquid-Fe₂O₃ used as carries, *Polyc. Arom. Comp.* 40 (3) (2020) 574–584.
- [18] Y. Wang, W. Lou, X. Wang, A green way to synthesize lubricating ester oils: The esterification of pentaerythritol with fatty acids at stoichiometric ratio over [BHSO₃MMIm]⁺[HSO₄]⁻/SiO₂, *Catal. Commun.* 111 (2018) 21–25.
- [19] H.-C. Chang, T.-H. Wang, C.M. Burba, Probing structures of interfacial 1-butyl-3-methylimidazolium trifluoromethanesulfonate ionic liquid on nano-aluminum oxide surfaces using high-pressure infrared spectroscopy, *Appl. Sci.* 7 (2017) 855.
- [20] I. Tankov, R. Yankova, A. Veli, R. Nikolova, Z. Mustafa, I. Stoycheva, Effect of the active phase-support interaction on the electronic, thermal and catalytic properties of [H-Pyr]⁺[HSO₄]⁻/support (support = rice husk ash; corundum), *J. Mol. Liq.* 315 (2020) 113725.
- [21] X. Zhang, D. Sua, L. Xiaoa, W. Wu, Immobilized protic ionic liquids: Efficient catalysts for CO₂ fixation with epoxides, *J. CO₂ Utiliz.* 17 (2017) 37–42.
- [22] M.S. Raja Shahrom, A.R. Nordin, C.D. Wilfred, Activated carbon supported amine functionalized ionic liquids for CO₂ sorption, *J. Phys.: Conf. Series* 1123 (2018) 012069, <https://doi.org/10.1088/1742-6596/1123/1/012069>.
- [23] M. Yu, S. Zeng, Z. Wang, Z. Hu, H. Dong, Y. Nie, B. Ren, X. Zhang, Protic ionic-liquid-supported activated carbon with hierarchical pores for efficient NH₃ adsorption, *ACS Sustainable Chem. Eng.* 7 (2019) 11769–11777.
- [24] K.R. Maiyelvaganan, S. Kamalakannan, M. Prakash, Adsorption of ionic liquids on carbonaceous surfaces: The effect of curvature on selective anion- π and cation- π interactions, *Appl. Surf. Sci.* 495 (2019) 143538.
- [25] P. Losch, A.M. Pascual, M. Boltz, S. Ivanova, B. Louis, F. Montilla, J.A. Odriozola, Ionic liquid immobilization on carbon nanofibers and zeolites: Catalyst design for the liquid-phase toluene chlorination, *C. R. Chimie* 18 (2015) 324–329.
- [26] M. Saghraivaniana, M. Ebrahimia, Z. Es'haghi, S. Ali Beyramabadi, Experimental sensing and density functional theory study of an ionic liquid mediated carbon nanotube modified carbon-paste electrode for electrochemical detection of metronidazole, *S. Afr. J. Chem.* 70 (2017) 29–37.
- [27] M.H. Valkenberg, C. de Castro, W.F. Hölderich, Immobilisation of chloroaluminate ionic liquids on silica materials, *Top. Catal.* 14 (2001) 139–144.
- [28] Jean-Michel Andanson, Alfons Baiker, Interactions of 1-ethyl-3-methylimidazolium trifluoromethanesulfonate ionic liquid with alumina nanoparticles and organic solvents studied by infrared spectroscopy, *J. Phys. Chem. C* 117 (23) (2013) 12210–12217.
- [29] Ivaylo Tankov, Romyana Yankova, A combined DFT and FT-IR study on the surface interactions in alumina supported ionic liquid [H-Pyr]⁺[HSO₄]⁻, *Spectrochim. Acta Part A: Mol. Biomol. Spectrosc.* 226 (2020) 117545, <https://doi.org/10.1016/j.saa.2019.117545>.
- [30] János Végh, The Shirley background revised, *J. Electron Spectrosc. Relat. Phenom.* 151 (3) (2006) 159–164.
- [31] J.H. Scofield, Hartree-Slater subshell photoionization cross-sections at 1254 and 1487 eV, *J. Electron Spectrosc. Relat. Phenom.* 8 (2) (1976) 129–137.

- [32] Huishan Shang, Yanjie Lu, Feng Zhao, Cong Chao, Bing Zhang, Hongsong Zhang, Preparing high surface area porous carbon from biomass by carbonization in a molten salt medium, *RSC Adv.* 5 (92) (2015) 75728–75734.
- [33] M. Hu, Z. Yao, X. Wang, Characterization techniques for graphene-based materials in catalysis, *AIMS Mater. Sci.* 4 (3) (2017) 755–788.
- [34] S. Sonal, P. Prakash, B.K. Mishra, G.C. Nayak, Synthesis, characterization and sorption studies of a zirconium(IV) impregnated highly functionalized mesoporous activated carbons, *RSC Adv.* 10 (2020) 13783–13798.
- [35] Tian Qiu, Jian-Guo Yang, Xue-Jie Bai, Yu-Ling Wang, The preparation of synthetic graphite materials with hierarchical pores from lignite by one-step impregnation and their characterization as dye absorbents, *RSC Adv.* 9 (22) (2019) 12737–12746.
- [36] Magdalena Zięzio, Barbara Chermas, Katarzyna Jedynak, Monika Hawryluk, Karolina Kucio, Preparation and characterization of activated carbons obtained from the waste materials impregnated with phosphoric acid(V), *Appl. Nanosci.* 10 (12) (2020) 4703–4716.
- [37] R. Siburian, H. Sihotang, S. Lumban Raja, M. Supeno, C. Simanjuntak, New route to synthesize of graphene nano sheets, *Orient. J. Chem.* 34 (1) (2018) 182–187.
- [38] Md Shariful Islam, Bee Chin Ang, Samira Gharehkhani, Amalina Binti Muhammad Afifi, Adsorption capability of activated carbon synthesized from coconut shell, *Carbon Lett.* 20 (2016) 1–9.
- [39] Robin D. Rogers, Cary B. Bauer, Crystal structure of pyridinium hydrogen sulfate, $[\text{HC}_5\text{H}_5\text{N}][\text{HSO}_4]$, *J. Chem. Crystallogr.* 24 (4) (1994) 285–287.
- [40] H. Badenhorst, Microstructure of natural graphite flakes revealed by oxidation: Limitations of XRD and Raman techniques for crystallinity estimates, *Carbon* 66 (2014) 674–690.
- [41] I. Tankov, K. Arishtirova, J.M.C. Bueno, S. Damyanova, Surface and structural features of Pt/PrO₂-Al₂O₃ catalysts for dry methane reforming, *Appl. Catal. A: General* 474 (2014) 135–148.
- [42] I. Tankov, B. Pawelec, K. Arishtirova, S. Damyanova, Structure and surface properties of praseodymium modified alumina, *Appl. Surf. Sci.* 258 (1) (2011) 278–284.
- [43] M. Thommes, K. Kaneko, A.V. Neimark, J.P. Olivier, F. Rodriguez-Reinoso, J. Rouquerol, K.S.W. Sing, Physisorption of gases, with special reference to the evaluation of surface area and pore size distribution (IUPAC Technical Report), *Pure Appl. Chem.* 87 (9–10) (2015) 1051–1069.
- [44] Toshihide Horikawa, D.D. Do, D. Nicholson, Capillary condensation of adsorbates in porous materials, *Adv. Colloid Interf. Sci.* 169 (1) (2011) 40–58.
- [45] T. Ramesh, N. Rajalakshmi, K.S. Dhathathreyan, Synthesis and characterization of activated carbon from jute fibers for hydrogen storage, *Renew. Energy Environ. Sustain.* 2 (2017) 4.
- [46] Artur P. Terzyk, The influence of activated carbon surface chemical composition on the adsorption of acetaminophen (paracetamol) in vitro Part II. TG, FTIR, and XPS analysis of carbons and the temperature dependence of adsorption kinetics at the neutral pH, *Colloid, Surf. A: Physicochem. Eng. Aspects* 177 (1) (2001) 23–45.
- [47] B. Bonelli, B. Onida, B. Fubini, C. Otero Areán, E. Garrone, Vibrational and thermodynamic study of the adsorption of carbon dioxide on the zeolite Na-ZSM-5, *Langmuir* 16 (11) (2000) 4976–4983.
- [48] Kristi L. Kauffman, Jeffrey T. Culp, Angela Goodman, Christopher Matranga, FT-IR Study of CO₂ adsorption in a dynamic copper(II) benzoate-pyrazine host with CO₂-CO₂ interactions in the adsorbed state, *J. Phys. Chem. C* 115 (5) (2011) 1857–1866.
- [49] Jurgis Barkauskas, Maryte Dervinyte, An investigation of the functional groups on the surface of activated carbons, *J. Serb. Chem. Soc.* 69 (5) (2004) 363–375.
- [50] Sumrit Mopoung, Phansiri Moonsri, Wanwimon Palas, Sataporn Khumpai, Characterization and properties of activated carbon prepared from tamarind seeds by KOH activation for Fe(III) adsorption from aqueous solution, *Sci. World J.* 2015 (2015) 1–9.
- [51] G. Wang, C. Feng, Electrochemical polymerization of hydroquinone on graphite felt as a pseudo capacitive material for application in a microbial fuel cell, *Polymers* 9 (2017) 220.
- [52] S.M. Anisuzzaman, Collin G. Joseph, Y.H. Taufiq-Yap, Duduku Krishnaiah, V.V. Tay, Modification of commercial activated carbon for the removal of 2,4-dichlorophenol from simulated wastewater, *J. King Saud Univ.* 27 (4) (2015) 318–330.
- [53] Saeedeh Hashemian, Khaterah Salari, Hamila Salehifar, Zahra Atashi Yazdi, Removal of azo dyes (violet b and violet 5r) from aqueous solution using new activated carbon developed from orange peel, *J. Chem.* 2013 (2013) 1–10.
- [54] Hui Deng, Guoxue Li, Hongbing Yang, Jiping Tang, Jiangyun Tang, Preparation of activated carbons from cotton stalk by microwave assisted KOH and K₂CO₃ activation, *Chem. Eng. J.* 163 (3) (2010) 373–381.
- [55] A.H. Wazir, I.W. Kundi, Synthesis of graphene nano sheets by the rapid reduction of electrochemically exfoliated graphene oxide induced by microwaves, *J. Chem. Soc. Pak.* 38 (1) (2016) 11–16.
- [56] H.N. Tran, F.-C. Huang, C.-K. Lee, H.-P. Chao, Activated carbon derived from spherical hydrochar functionalized with triethylenetetramine: synthesis, characterizations, and adsorption application, *Green Process Synth.* 6 (2017) 565–576.
- [57] G.F. de Oliveira, R.C. de Andrade, M.A.G. Trindade, H.M.C. Andrade, C.T. de Carvalho, Thermogravimetric and spectroscopic Study (TG-DTA/FT-IR) of activated carbon from the renewable biomass source babassu, *Quim. Nova* 40 (3) (2017) 284–292.
- [58] T. Seki, K.-Y. Chiang, C.-C. Yu, X. Yu, M. Okuno, J. Hunger, Y. Nagata, M. Bonn, The bending mode of water: a powerful probe for hydrogen bond structure of aqueous systems, *J. Phys. Chem. Lett.* 11 (2020) 8459–8469.
- [59] J.-H. Choi, M. Cho, Computational IR spectroscopy of water: OH stretch frequencies, transition dipoles, and intermolecular vibrational coupling constants, *J. Chem. Phys.* 138 (2013) 174108.
- [60] D. Gandolfo, J. Zarembowitch, Apport de la coordination des heterocycles a la connaissance de leurs spectres infrarouge et Raman. III-Spectres de lamethyl-3 pyridine, *Spectrochim. Acta* 33 (1977) 615–623.
- [61] A. Periasamy, S. Muruganand, M. Palaniswamy, Vibrational studies of Na₂SO₄, K₂SO₄, Na-HSO₄ and KHSO₄ crystals, *Rasayan J. Chem.* 2 (4) (2009) 981–989.
- [62] Y. Zhang, H. He, S. Zhang, M. Fan, Hydrogen-bonding interactions in pyridinium-based ionic liquids and dimethyl sulfoxide binary systems: a combined experimental and computational study, *ACS Omega* 3 (2018) 1823–1833.
- [63] Reza Tayebee, Malihe Jomei, Behrooz Maleki, Maryam Kargar Razi, Hojat Veisi, Mohammad Bakherad, A new natural based ionic liquid 3-sulfonic acid 1-imidazolopyridinium hydrogen sulfate as an efficient catalyst for the preparation of 2H-indazole[2,1-b]-phthalazine-1,6,11(13H)-triones, *J. Mol. Liq.* 206 (2015) 119–128.
- [64] F. Zhou, H.N. Tien, W.L. Xu, J.-T. Chen, Q. Liu, E. Hicks, M. Fathizadeh, S. Li, M. Yu, Ultrathin graphene oxide-based hollow fiber membranes with brush-like CO₂-philic agent for highly efficient CO₂ capture, *Nat. Commun.* 8 (2017) 2107.
- [65] Jana Tabačiarová, Matej Mičušík, Pavol Fedorko, Mária Omastová, Study of polypyrrole aging by XPS, FTIR and conductivity measurements, *Polym. Degr. Stab.* 120 (2015) 392–401.
- [66] A. Azioune, A.B. Slimane, L.A. Hamou, A. Pleuvy, M.M. Chehimi, C. Perruchot, S. P. Armes, Synthesis and characterization of active ester-functionalized polypyrrole-silica nanoparticles: Application to the covalent attachment of proteins, *Langmuir* 20 (2004) 3350–3356.
- [67] A. Dolgov, D. Lopaev, C.J. Lee, E. Zoethout, V. Medvedev, O. Yakushev, F. Bijkerk, Characterization of carbon contamination under ion and hot atom bombardment in a tin-plasma extreme ultraviolet light source, *Appl. Surf. Sci.* 353 (2015) 708–713.
- [68] A. Foelske-Schmitz, D. Weingarth, R. Kötz, XPS analysis of activated carbon supported ionic liquids: Enhanced purity and reduced charging, *Surf. Sci.* 605 (2011) 1979–1985.
- [69] Mok-Hwa Kim, Sol Yun, Ho Seok Park, Joong Tark Han, Kwang-Bum Kim, Kwang Chul Roh, Retransformed graphitic activated carbon from ionic liquid-derived carbon containing nitrogen, *J. Mater. Chem. A* 3 (6) (2015) 2564–2567.
- [70] Rad Sadri, Maryam Hosseini, S.N. Kazi, Samira Bagheri, Nashrul Zubir, K.H. Solangi, Tuan Zaharinie, A. Badarudin, A bio-based, facile approach for the preparation of covalently functionalized carbon nanotubes aqueous suspensions and their potential as heat transfer fluids, *J. Coll. Interf. Sci.* 504 (2017) 115–123.
- [71] J.A. Leiroa, M.H. Heinonen, T. Laiho, I.G. Batirev, Core-level XPS spectra of fullerene, highly oriented pyrolytic graphite, and glassy carbon, *J Electron Spectrosc Relat Phenomena* 128 (2003) 205–213.
- [72] Ling Zhang, Ling-yu Tu, Yan Liang, Qi Chen, Ze-sheng Li, Chun-hai Li, Zhi-hui Wang, Wen Li, Coconut-based activated carbon fibers for efficient adsorption of various organic dyes, *RSC Adv.* 8 (74) (2018) 42280–42291.
- [73] M. Wahlgvist, A. Shchukarev, XPS spectra and electronic structure of Group IA sulfates, *J. Electr. Spectrosc. Relat. Phenomena* 156–158 (2007) 310–314.
- [74] Vaithiyalingam Shutthanandan, Manjula Nandasiri, Jianming Zheng, Mark H. Engelhard, Wu Xu, Suntharampillai Thevuthasan, Vijayakumar Murugesan, Applications of XPS in the characterization of Battery materials, *J. Electr. Spectrosc. Relat. Phenomena* 231 (2019) 2–10.
- [75] Y. Zhang, K. Dong, Z. Liu, H. Wang, S. Ma, A. Zhang, M. Li, L. Yu, Y. Li, Sulfurized hematite for photo-Fenton catalysis, *Progr. Nat. Sci.: Mater. Int.* 27 (2017) 443–451.
- [76] Masamitsu Watanabe, Hiroshi Ando, Takao Handa, Toshihiro Ichino, Nobuo Kuwaki, Comparative XPS study of silver and copper surfaces exposed to flowing air containing low concentration of sulfur dioxide, *Zairyo-to-Kankyo* 56 (1) (2007) 10–15.
- [77] Hans-Peter Steinrück, Recent developments in the study of ionic liquid interfaces using X-ray photoelectron spectroscopy and potential future directions, *Phys. Chem. Chem. Phys.* 14 (15) (2012) 5010, <https://doi.org/10.1039/c2cp24087d>.
- [78] S. Kabir, K. Artyushkova, A. Serov, B. Kiefer, P. Atanassov, Binding energy shifts for nitrogen-containing graphene-based electrocatalysts – experiments and DFT calculations, *Surf. Interface Anal.* 48 (5) (2016) 293–300.
- [79] R. Yankova, I. Tankov, Chemical reactivity of the ionic liquid tris(2-amino-1,3-thiazolium) hydrogen sulfate sulfate monohydrate (TAHSSM) and surface effects in the TAHSSM/α-Al₂O₃ system, *323* (2021) 114634.
- [80] Ivaylo Tankov, Romyana Yankova, Quantum mechanical and reaction dynamics investigation of butyl acetate synthesis in the presence of pyridinium hydrogen sulfate, *J. Mol. Liq.* 278 (2019) 183–194.
- [81] Ivaylo Tankov, Romyana Yankova, DFT analysis, reaction kinetics and mechanism of esterification using pyridinium nitrate as a green catalyst, *J. Mol. Liq.* 277 (2019) 241–253.
- [82] Ivaylo Tankov, Romyana Yankova, Theoretical (density functional theory) studies on the structural, electronic and catalytic properties of the ionic liquid 4-amino-1H-1,2,4-triazolium nitrate, *J. Mol. Liq.* 269 (2018) 529–539.
- [83] I. Tankov, M. Mitkova, R. Nikolova, A. Veli, D. Stratiev, n-Butyl acetate synthesis in the presence of pyridinium-based acidic ionic liquids: influence of the anion nature, *Catal. Lett.* 147 (2017) 2279–2289.

- [84] Jose Scillipoti, Claudia Nioi, Alain Marty, Séverine Camy, Jean-Stephane Condoret, Prediction of conversion at equilibrium for lipase esterification in two-phase systems, *Biochem. Eng. J.* 117 (2017) 162–171.
- [85] N.S.A. Zeki, M.H. Al-Hassani, H.A. Al-Jendeel, Kinetic study of esterification reaction, *Al-Khwarizmi Eng. J.* 6 (2) (2010) 33–42.
- [86] J. Vojtko, J. Durdiak, Z. Lukáčová-Chomisteková, P. Tomčík, Prediction of esterification rate constants for secondary alkan-2-ols based on one- and two-parameter Taft equations, *Prog. React. Kinet. Mec.* 45 (2020) 1–9.
- [87] Edward Sarlo, Paris Svoronos, Patricia Kulas, Calculation of equilibrium constant in esterification reactions, *J. Chem. Educ.* 67 (9) (1990) 796, <https://doi.org/10.1021/ed067p796>.
- [88] F.F. Bamoharram, M.M. Heravi, P. Ardalan, T. Ardalan, A kinetic study of the esterification of lactic acid by ethanol in the presence of Preyssler acid an eco-friendly solid acid catalyst, *Reac Kinet Mech Cat* 100 (2010) 71–78.
- [89] P. Atkins, L. Jones, *Chemical Principles: The Quest for Insight*. W H Freeman & Co. ISBN 978-1-4292-0965-6 (2007).
- [90] Piret Villo, Oscar Dalla-Santa, Zoltán Szabó, Helena Lundberg, Kinetic analysis as an optimization tool for catalytic esterification with a moisture-tolerant zirconium complex, *J. Org. Chem.* 85 (11) (2020) 6959–6969.
- [91] Ramakrishnan Radhakrishnan, Sivakumar Thiripuranthagan, Arulselvan Devarajan, Sakthivel Kumaravel, Elangovan Erusappan, Kathiravan Kannan, Oxidative esterification of furfural by Au nanoparticles supported CMK-3 mesoporous catalysts, *Appl. Catal. A Gen.* 545 (2017) 33–43.
- [92] P.E. JagadeeshBabu, K. Sandesh, M.B. Saidutta, Kinetics of esterification of acetic acid with methanol in the presence of ion exchange resin catalysts, *Ind. Eng. Chem. Res.* 50 (2011) 7155–7160.
- [93] Sema Akyalçın, Mehmet Rıza Altıokka, Kinetics of esterification of acetic acid with 1-octanol in the presence of Amberlyst 36, *Appl. Catal. A Gen.* 429–430 (2012) 79–84.
- [94] Aspi K. Kolah, Navinchandra S. Asthana, Dung T. Vu, Carl T. Lira, Dennis J. Miller, Reaction kinetics for the heterogeneously catalyzed esterification of succinic acid with ethanol, *Ind. Eng. Chem. Res.* 47 (15) (2008) 5313–5317.
- [95] Koshiro Nakamura, Ryo Mizuta, Satoshi Sugauma, Etsushi Tsuji, Naonobu Katada, Compensation between activation entropy and enthalpy in reactions of aromatic hydrocarbons catalyzed by solid acids, *Catal. Commun.* 102 (2017) 103–107.